

FABRIC ANALYSIS OF SURVIVOR CLASTS IN THE SOUTHWEST DEFORMING
ZONE OF THE SAN ANDREAS FAULT AT THREE KILOMETERS DEPTH

A Thesis

by

AILEEN LOFTIN

Submitted to the Office of Graduate and Professional Studies of
Texas A&M University
in partial fulfillment of the requirements for the degree of

MASTER OF SCIENCE

Chair of Committee,	Frederick M. Chester
Co-Chair of Committee,	Judith S. Chester
Committee Member,	John R. Giardino
Head of Department,	John R. Giardino

December 2014

Major Subject: Geophysics

Copyright 2014 Aileen Loftin

ABSTRACT

The mechanisms responsible for aseismic creep along the central section of the San Andreas Fault are not well understood. Evidence for both pressure- and chemical-dependent microprocesses of creep have been reported. Here, the kinematics and deformation mechanisms of the Southwest Deforming Zone (SDZ) of the San Andreas Fault are investigated through fabric analysis of survivor clasts recovered from ~2.6 km depth by coring at the San Andreas Fault Observatory at Depth (SAFOD).

The size-frequency and shape-size distributions of survivor clasts from the SDZ were characterized through 3D analysis of X-Ray Computed Tomography (XCT) images of SDZ core samples. A number of processing techniques were employed to calibrate, remove artifacts, filter and threshold the XCT images and distinguish survivor clasts so as to enable 3D rendering of clasts for size and shape analysis. The size of clasts fit a power-law probability distribution function with a negative exponent (scaling parameter) of 3 over the range of 0.45 mm to 60 mm in diameter. Using best-fit primitive ellipsoids and clast volume as reference, clast shapes are characterized as oblate spheroids, moderate (1.5-2.5) aspect ratio with high convexity and sphericity (>0.6); the shape distributions appear invariant with clast size.

The size and shape characteristics, and the uniform spatial distribution of survivor clasts within the SDZ, suggest that the zone has attained a mature, quasi steady-state condition. The scaling parameter of 3 supports that the reduction in the size of clasts is a result of fracture consistent with a nearest neighbor fragmentation model for

high strain, matrix-dominated shear zones. However, clast shape distributions support that surface wear, such as by abrasion or pressure solution, are the dominant clast shaping process.

ACKNOWLEDGEMENTS

I would like to thank my committee co-chairs, Dr. Frederick M. Chester and Dr. Judith S. Chester, for their guidance and support throughout the course of this research.

Thanks also go to my friends and colleagues and the department faculty and staff for making my time at Texas A&M University a great experience.

Finally, thanks to my husband for his encouragement and to my son for his patience and love.

TABLE OF CONTENTS

	Page
ABSTRACT	ii
ACKNOWLEDGEMENTS	iv
TABLE OF CONTENTS	vi
LIST OF FIGURES.....	vii
LIST OF TABLES	ix
1. INTRODUCTION.....	1
2. DESCRIPTION OF STUDY AREA.....	6
2.1. The San Andreas Fault at SAFOD	6
2.2. G2S7 Core Description	6
2.3. Fabricated Sample Description	7
3. PARTICLE SIZE AND SHAPE ANALYSIS METHODS	8
3.1. X-ray Computed Tomography Scanning	8
3.2. Image Analysis.....	9
3.3. Particle Size Analysis.....	13
3.4. Particle Shape Analysis.....	15
4. RESULTS.....	17
4.1. Classification of Size and Shape	17
4.2. Distribution of Clasts in the Gouge.....	18
4.3. Clast and Matrix Volume in the Gouge of the SDZ.....	19
4.4. Particle Size Distributions.....	19
4.5. Clast Shape.....	21
5. DISCUSSION	25
5.1. Insights into Deformation Based on Survivor Clast Size.....	25
5.2. Insights into Deformation Based on Survivor Clast Shape.....	28
5.3. Quasi Steady-state Condition.....	30

5.4. Similarities in the SDZ and CDZ.....	30
6. CONCLUSIONS.....	32
6.1. Findings.....	32
6.2. Conclusions.....	33
REFERENCES.....	34
APPENDIX A.....	39
APPENDIX B.....	66
APPENDIX C.....	73
APPENDIX D.....	77

LIST OF FIGURES

FIGURE	Page
1. Map of California showing the locations of SAFOD, the creeping section, and locked sections of the San Andreas Fault, a continental transform fault that has accommodated hundreds of kilometers of relative motion between the North American Plate and the Pacific Plate	40
2. A cross section illustrating the SAFOD borehole geometry and identifying the three phases of drilling [modified from <i>Chester et al.</i> , 2008 and <i>Sills</i> , 2010	41
3. Photographic image of the surface of a portion of the G2S7 core from the SDZ that was scanned for this study [modified from J. S. Chester.....	42
4. Schematic diagram showing the dimensions and composition of the cores scanned by XCT in scan series A, B, and F	42
5. Collection of XCT images illustrating image processing techniques applied to scan series A and B images using code written in Matlab	44
6. Set of XCT images showing the effects of image processing techniques applied to series A and B.....	45
7. Collection of XCT scans illustrating image processing techniques applied to series F using code written in Matlab	46
8. A 3D reconstructed blob showing two joined clasts that must be manually separated prior to size analysis.....	47
9. Example values of sphericity, convexity, and elongation for different 2D particle shapes	47
10. Distribution of acceptable, useable, and excluded clasts for particle size and shape quality classification as a function of cumulative number of clasts analyzed starting with the largest clast.....	49
11. Spatial distribution of clasts within the foliated gouge in the SDZ as a function of clast-size range.....	50
12. Particle size distribution of clasts within the scan series F of the SDZ comparing data sets with and without the excluded clasts.....	51

13. Particle size distribution for clasts within the SDZ at two scale ranges.....	52
14. Particle size distribution for clasts within the SDZ from scan series F showing the portion of the data set that fits a power law distribution based on the method of <i>Clauset et al.</i> [2009]	53
15. Particle size distribution plot for survivor clasts within the SDZ and CDZ over the same scale range.....	55
16. Composite particle size distribution plot for survivor clasts within the SDZ over three scale ranges	56
17. Shape of best-fit primitive ellipsoids to survivor clasts from the SDZ for series A, B, and F plotted in a Flinn diagram.....	57
18. Shape of best-fit primitive ellipsoids to survivor clasts from the SDZ for series A, B, and F plotted in a Zingg diagram.....	58
19. Scatter plots of log equivalent spherical diameter versus convexity for survivor clasts from the SDZ for series A, B, and F	61
20. Scatter plots of log equivalent spherical diameter versus sphericity for survivor clasts from the SDZ for series A, B, and F	62
21. Sample of clast shapes with corresponding sphericity values.....	63
22. Scatter plots of log equivalent spherical diameter versus sphericity showing the result of adding the excluded clasts to the data sets of scan series A, B, and F of the SDZ	64

LIST OF TABLES

TABLE	Page
1. XCT Images (slices) covering units of SDZ G2S7 core for series A and B	43
2. Blob3D Input parameters used for 3D reconstruction of clast.....	48
3. Particle size distribution results.....	54
4. Comparison of particle size parameters with and without excluded clasts...	57
5. Classification and distribution of clast shape	59
6. Shape parameters percentages by value ranges.....	60
7. Shape distributions with 99.9% confidence where value of 0 is statistically the same and value of 1 is statistically different	64
8. File naming convention.....	65

1. INTRODUCTION

There are many mechanisms that achieve slip within large displacement faults [e.g., *Sibson*, 1977, 1986]. For faults that creep aseismically, it is possible that creep is accommodated by brittle processes alone [e.g., fracturing, comminution, frictional sliding], but normally chemical and temperature activated processes of pressure solution, dislocation creep, and diffusion creep [*Sibson*, 1977; *Mei & Kohlstedt*, 2000a; *Mei & Kohlstedt*, 2000b] are invoked, as well as calling on the alteration of minerals [*Wu*, 1975] and increase in pore fluid pressure [*Sibson*, 1973]. Even for intensely studied faults like the San Andreas Fault, a major plate-boundary fault, we do not completely understand what leads to aseismic creep and seismic slip on different portions of the fault. Knowledge of the contributing mechanisms is crucial to understanding deformation and slip mode along plate boundaries.

The San Andreas Fault is a complex fault system forming the transform boundary between the Pacific plate to the west and the North American plate to the east (Figure 1). Faults of the system experience both steady state creep and episodic seismic slip. The central creeping section (aseismic creep rates of approximately 2.5 cm/year; *Titus et al.*, 2006) is bounded by two locked sections (Figure 1). The presence of weak minerals formed by mineral transformation points to the role of chemical reactions within the creeping segment of the San Andreas Fault [*Moore & Rymer*, 2007; *Lockner et al.*, 2011; *Moore & Rymer*, 2012; *Moore & Lockner*, 2013]. Evidence of both pressure dependent (e.g., fracture) and chemical dependent processes (pressure solution) have

been reported for the actively creeping zones [*Mittempergher et al.*, 2011; *Moore & Rymer*, 2012; *Moore & Lockner*, 2013]. Although a number of different approaches have been used to study deformation processes in the San Andreas Fault, few studies have attempted to differentiate processes through fabric analysis of survivor clasts within gouge [*Sills*, 2010].

Particle size analysis of the survivor clasts could contribute to the understanding of the deformation mechanisms observed in actively creeping zones of faults [*Marone & Scholz*, 1989; *An & Sammis*, 1994; *Sammis & King*, 2007]. Particle size distributions of San Andreas fault gouge [*Sills*, 2010] and other fault rocks [*Sammis et al.*, 1987, *Marone & Scholz*, 1989; *An & Sammis*, 1994; *Heilbronner & Keulen*, 2006; *Keulen et al.*, 2007; *Bjork et al.*, 2009], fit to a power law probability distribution, have been used to discriminate mechanisms of deformation. Many models have been proposed to explain gouge generation by grain comminution, grinding, attrition, and shear during slip along a fault zone [*Sammis et al.*, 1987; *Sammis and King*, 2007, *Keulen et al.*, 2007; *Sills*, 2010; *Heron*, 2011]. Grain size distributions of granitoid fault rocks have been used to document the operation of multiple mechanisms, and a change in the dominant process with a reduction of scale. Specifically, the observation of an abrupt change in the scaling parameter of a power law size distribution is inferred to represent a change in comminution mechanism; a less negative parameter for grains smaller than $\sim 2 \mu\text{m}$ describes attrition processes and a more negative scaling parameter for the larger grains describes grain size reduction by fragmentation during grinding.

Evidence for concurrent operation of different processes may exist, but often it is difficult to determine which process controls or is responsible for the slip behavior because the signature of a process may be subtle or not well-preserved in the rock record, or the signatures may be overprinted by subsequent deformation or mineral reactions. In addition, it is simply difficult to acquire samples at depth from active faults that are known to be slipping seismically or aseismically.

Scientific drilling at the San Andreas Fault Observatory at Depth (SAFOD) has provided core samples from an actively creeping aseismic zone at ~2.6 km depth. In particular, core samples recovered from across the two actively creeping zones, the Central Deforming Zone (CDZ) and the Southwest Deforming Zone (SDZ), document that the creep is taking place with meters-thick layers of clay-rich fault gouge. The CDZ and SDZ gouge characteristically contains a small volume fraction of survivor clasts of the wall rock that tend to be supported by the clay rich matrix of the gouge. The purpose of this study is to use the size and shape characteristics of the survivor clasts within the gouge samples to constrain the processes operating in these deforming zones and to determine the likely controlling mechanisms.

Previous fabric analysis of survivor clasts in the CDZ and SDZ by *Sills* [2010] supports the hypothesis that aseismic creep in the SDZ and CDZ is related to distributed shearing of the fault rock. In particular, particle size-, shape-, and spatial-distribution analyses using both high (1024 x 1024 pixels) and low (512 x 512 pixels) resolution X-Ray Computed Tomography (XCT) scans of gouge from the CDZ lead *Sills* [2010] to infer frictional sliding in the gouge produced a strong shape preferred orientation of the

clasts. *Sills* [2010] also conducted analyses of low resolution (512 x 512 pixels) images of the SDZ. The study determined that the size-frequency distribution of clasts in 3D fit a power law with an exponent of approximately -3 for clasts ranging from 60 – 6 mm equivalent diameter, similar to size-frequency relations seen in some other fault gouge studies [*Marone & Scholz, 1989; An & Sammis, 1994; Heilbronner & Keulen, 2006; Bjork et al., 2009; Sills, 2010*]. A power law scaling parameter of -3 implies that constrained fracturing of similar-sized nearest-neighbors is not the dominant clast-size reduction mechanism [*Sammis & King, 2007*]. Although particle size analysis of the SDZ at low resolution was carried out by *Sills* [2010], it is not known if the determined scaling also describes the population of survivor clasts that are less than 6 mm in diameter. Generally, there have been infrequent attempts in the literature to evaluate naturally occurring upper and lower cutoffs to observed power law distributions [*Bonnet et. al., 2001*].

Sills [2010] described survivor clasts in the SDZ and CDZ as lenticular-shaped clasts using qualitative observations of acute angles and delicate edges. Additionally, *Sills* [2010] categorized the clasts as oblate spheroids based on a qualitative first order approximation of the aspect ratio using best fit ellipsoids. Although this qualitative method is widely accepted, a quantitative shape analysis in combination with particle size analysis is needed in order to better discriminate between deformation processes operating within the fine clayey matrix of the fault gouge. Following this previous work, the present study will attempt to discriminate between the two working hypotheses, that:

- (1) There is a change in the clast-size reduction mechanism from brittle fracturing to

pressure solution with a decrease in clast size; (2) Pressure solution may become more important for smaller sized clasts, but it does not become dominant in controlling either the size or shape distributions.

Most previous studies of particle size distributions in fault rocks have not demonstrated whether the power law is the most appropriate probability distribution, nor whether the scaling parameter (exponent of the power law) can discriminate between different deformation processes. A secondary goal of this work is to employ a recently developed statistical framework for discerning and quantifying power-law behavior in empirical data, as well as identifying the range over which the power law holds [*Clauset et al.*, 2009]. By gathering new clast-size and -shape data over an even broader range of clast sizes, and employing a robust statistical approach to the size distribution analysis, combined with quantitative clast-shape analysis as a function of scale of observation, the understanding of mechanisms operative in the creeping zones of the San Andreas Fault is advanced.

2. DESCRIPTION OF STUDY AREA

2.1. San Andreas Fault at SAFOD

The San Andreas Fault Observatory at Depth (SAFOD), located at the southern end of the creeping segment of the San Andreas Fault near Parkfield, California (Figure 1), primarily consists of an inclined borehole that transects the active trace of the San Andreas Fault at 2.5 to 2.7 km depth. The borehole was completed during three phases of drilling (Figure 2). During phase 3, spot core was acquired from the two actively creeping zones of the fault, the Southwest Deforming Zone (SDZ) and the Central Deforming Zone [CDZ; *Zoback et al.*, 2011]. Both actively creeping zones contain meters-thick gouge layers consisting of approximately 80% clay-bearing, ultrafine grain gouge containing survivor clasts (referred to as clasts hereafter) from the host wall-rock [e.g., *Moore & Rymer*, 2007].

This study targets the SDZ to examine the structure of survivor clasts within an actively creeping fault gouge zone. Two sections of core (#7 and #8 from Hole G, Coring Run 2; the G2S7 and G2S8 cores) are used to characterize the size and shape of survivor clasts within the foliated gouge.

2.2. G2S7 Core Description

The foliated gouge is composed of ultra-fine grain silt and clay-sized matrix. Within the foliated gouge are survivor clasts composed of siltstone, mudstone, serpentinite and calcite veins from the surrounding wall rocks. The composition of the portion of the G2S7 core used for this research is summarized in Table 1. A

photographic image of this portion of the core is shown in Figure 3. A schematic diagram of the G2S7 core is presented in Figure 4.

2.3. Fabricated Sample Description

The fabricated sample is composed of waste fragments of foliated gouge from the G2S8 core. The sample was constructed by lightly packing fragments in a cylindrical polyolefin tube 32.63 mm in length, 25.4 mm in diameter, and 1 mm wall thickness; the cylinder was filled with epoxy to saturate the fragments and fill all pore space. A schematic diagram of the fabricated sample is presented in Figure 4.

3. PARTICLE SIZE AND SHAPE ANALYSIS METHODS

3.1. X-Ray Computed Tomography Scanning

X-Ray Computed Tomography (XCT) scanning is a technique used in science and medicine to examine the internal 3D structure of solid objects in a non-destructive fashion. This technique measures radiodensity throughout the volume, where radiodensity reflect primarily the density of the material and secondarily the elemental composition; dark or low values of radiodensity reflect low density material. The scanning process results in a series of 2D image (slices) separated by a specified spacing increment, or inter-slice spacing. To examine survivor clasts in a gouge matrix, XCT images from Phase 3 core of the SDZ were collected at the High-Resolution X-Ray Computed Tomography Facility at The University of Texas at Austin (UTCT).

The XCT image scans were taken of the entire G2S7 core, at 400 kV and 3.7 mA, and have a 1024 x 1024 pixel resolution resulting in an inter-pixel spacing of 0.116 mm. Image slices were acquired perpendicular to the core axis every 0.45 mm, so that each voxel element, a three-dimensional pixel, is 0.116 mm x 0.116 mm x 0.45 mm. The portion of the core relevant to this study was scanned in two sections referred to as scan series A and series B. The diameter of the core and surrounding 5 mm thick aluminum sleeve is approximately 118 mm. The fabricated sample was imaged in a single series scan (scan F) to resolve smaller clasts (0.15 to 10 mm). Series F images have an inter-pixel spacing of 0.0266 mm (1024 x 1024 pixel resolution) and an inter-slice spacing of

0.02892 mm resulting in nearly cubic voxels 0.0266 mm x 0.0266 mm x 0.0289 mm. The XCT images for all three scan series are 16-bit grayscale Tiff images.

To determine particle size and shape from the XCT images in an automated fashion, each slice is calibrated, artifacts are removed, and images are thresholded to make binary images that illuminate just the survivor clasts. The binary slices are processed in Blob3D, a software package available from the UTCT, which constructs 3D representations of the thresholded clasts (blobs) and quantifies size and shape measurements of the blobs.

3.2. Image Analysis

For automated analysis of the particle size and shape using the Blob3D software, it is necessary to pre-process the XCT image series in order to accurately delineate the clasts in a consistent and reproducible fashion and that preserves relative radiodensity values of pixels and the size and shape of the clasts as seen in the original (raw) images. The images are processed in multiple steps, and for each step the images must be calibrated to maintain consistent pixel values. Each image slice is calibrated by setting the values of two pixels to 0 and 65536, the minimum and maximum value in 16-bit images, and each slice is recalibrated after each of the following steps. The image series A and series B are processed the exact same way, while the slices in series F are processed slightly differently because of the way the sample was fabricated. Using Matlab, I wrote and implemented code (Appendix B) to process the slices in an automated fashion.

For series A and series B, the center (x,y) of the core is determined and all pixels outside the radius of the core (54 mm) are set to black to remove the aluminum sleeve (Figure 5b). Recognizing that the illumination of the images is not uniform, and that the pixel values are somewhat higher in the center and decrease axial-symmetrically from that point, the center (x,y) of illumination was determined so that the illumination correction could be properly aligned for each image. Both the center of the core and the center of illumination were determined and recorded every 20th slice to account for a gradual shift in the centers from slice to slice. To create the illumination-correction mask, I determined the radial profile of average apparent radiodensity for a subset of the slices, specifically for the image slices that display the least variation in density arising from the presence of larger clasts and fractures; the selected images serve best for documenting the density variation in each image arising only from the uneven illumination effects. The radial profiles of the subset of slices are averaged and then least-squares fit to a 2nd degree polynomial. The mask is created using the best fit 2nd degree polynomial equation (Figure 5c), and with the center of illumination of each image slice and illumination-correction mask are aligned, and the mask is subtracted from the calibrated image. After the illumination is corrected (Figure 5d), a median filter is applied to reduce noise pixilation. The median filter determines the median value for an image region of X and Y pixels and applies that value to the center point of the region, for each pixel in the image. Next, a threshold value is determined that distinguishes the lesser grayscale values of the gouge matrix from the greater grayscale values of the survivor clasts. Through trial and iteration, I determine appropriate

threshold values of 25186 and 25445 for series A and series B, respectively, that best capture the size and shape of the clasts while simultaneously minimizing illumination of noise in the surrounding matrix. Using these threshold values, a weighted-neighbor thresholding scheme was implemented to produce binary images of clasts (Figure 5e). The weighted-neighbor thresholding scheme compares a weighted average value of a 3 x 3 pixel region to the threshold value, and if the average value is greater than or less than the threshold value, the center pixel is converted to a value of 1 for clasts (white) and 0 for matrix (black), respectively. The resulting binary image preserves pixilated but accurate size and shape of clasts within each slice. A detailed description of the image processing method is presented as Appendix B. A side-by-side comparison of a calibrated image and of the illumination corrected image is shown in Figure 6.

For scan series F, both the fragments of gouge used to make up the cylindrical sample and the clasts within the fragments are easily resolved in the raw image slices. Many of the fragments are too small for studying clasts, so only the large fragments are used for analysis of clasts. Accordingly, a threshold grayscale value of 12680 (determined by trial and iteration) to distinguish the epoxy (lesser values) from fragments (greater values) was used to create binary images. For each image slice, all pixels with values less than the threshold are set to 0 (black) and all pixels with a value greater than the threshold are set to 1 (white). To produce a binary image of fragments that are white and epoxy set to black. The binary fragment image is then produced to set pixel values for all fragments smaller than a set size to black. The calibrated image (Figure 7b) is multiplied by the corresponding binary image of fragments (Figure 7c),

which sets all grayscale pixel values outside the fragment to black but retains the calibrated grayscale values for each pixel within the largest fragments (Figure 7d). The resulting grayscale images of the largest fragments are then processed to isolate the clasts following the same steps for series A and series B described above. Specifically, a median filter is applied, a threshold pixel value (13660) to separate grayscale matrix values from grayscale survivor clast values is determined, and the weighted neighbor threshold method is applied to produce the final image slices showing only the clasts (Figure 7f). A detailed description of the image processing is presented as Appendix C.

The final binary images (pixel values of 0s and 1s) of clasts for all scan series are examined in Blob3D, a UTCT software package used for quantitative analysis of high resolution XCT datasets. Blob3D stacks high-resolution image slices and allows the user to examine and measure up to thousands of discrete three-dimensional objects (blobs) based on connected voxels (dimensional pixels). For each series, series A, B, and F, the size of a voxel varies as a function of the inter-pixel spacing and the inter-slice spacing (Table 2). Blob3D software requires the user to accept or reject each object, and allows the user to manually separate objects (in this case, survivor clasts) that may be touching (Figure 8).

The resolution of the XCT imaging limits accurate characterization of the smallest particles. In order to accept only meaningful survivor clasts, a minimum connected voxel size of 165 is chosen such that the smallest size particle is 0.68 mm in volume-equivalent spherical diameter for series A and B. Similarly, for series F, a minimum connected voxel size of 165 is chosen such that the smallest size particle is

0.11 mm in volume-equivalent spherical diameter. This cut-off in connected voxel size effectively bypasses reconstruction of blobs from too few slices (e.g., <3) to adequately determine clast size and shape. The input parameters used are summarized in Table 2.

For each of the survivor clasts, the following parameters are reported: volume, surface area, and maximum, intermediate, and minimum radius of a primitive ellipsoid. Separately, the binary image of the largest fragments in scan series F also is analyzed in Blob3D to determine the total volume of the fragments, which is needed to normalize the clast-count data to compare particle size distribution determined from different volumes of material. Blob3D determines the volume of an object based on the number of connected voxels. The surface area of an object is calculated based on the isosurface surrounding the object voxels. The aspect ratio is the major axis length divided by the minor axis length of the primitive-fit ellipsoid, which is calculated based on minimizing the misfit between the primitive and blob surfaces, as discussed in the Blob3D User Manual. A detailed description of the data collected is presented as Appendix D.

3.3. Particle Size Analysis

I quantify the size of clasts in terms of volume-equivalent spherical diameter, which is commonly used for particle size distributions. This length is determined for the diameter of a perfect sphere with volume equal to the volume of the clast as,

$$D = \left(\frac{6}{\pi} V_P \right)^{\frac{1}{3}}$$

where V_P is the volume of the clast. The volume-equivalent spherical diameter will be henceforth referred to as “diameter”.

Cumulative frequency plots are used herein to analyze particle size distributions, specifically to determine if the data fits a power law distribution [e.g. *Sammis et al.*, 1987; *Bonnet et al.*, 2001; *Sills*, 2010]. A power law is employed to describe the size distributions of the clasts,

$$N(D) = aD^{-n}$$

where $N(D)$ is the number of clasts with size greater than D , and a and n are constants in which n is the scaling parameter.

To determine if the particle size distribution fits a power law, a quantitative approach in which the statistical methods presented by *Clauset et al.* [2009] are used. First, the clast size diameter is fit to a power-law model, which employs the maximum likelihood estimation to determine the scaling parameter (n) and lower bound (x_{min}). Then 1000 synthetic data sets are generated using the same n and x_{min} equal to those of the distribution that best fits the observed data. Each synthetic data set is individually fit to its own power law model and the Kolmogorov-Smirnov statistic is calculated for each one relative to its own model. The KS statistic measures the maximum distance, between the distributions of the observed data and the model. The maximum distance, d , is defined as

$$d = \max_{x \leq x_{min}} |S(x) - P(x)|$$

Where $S(x)$ is the observed data and $P(x)$ is the model. The goodness-of-fit, p , which counts the fraction of synthetic distances that are larger than the empirical distance is a conservatively a good fit if $p > 0.1$. Using open source code in Matlab written by *Clauset et al.* [2009], I was able to implement this statistical method to my data.

3.4. Particle Shape Analysis

I quantify the 3D shape of clasts in terms of form, roundness, and sphericity. Equancy, which describes equi-dimensional particles regardless of roundness or sphericity, is the form factor chosen to describe particle form. In terms of deviation from equancy, I follow the classification of degree of equancy defined by *Blott & Pye* [2008]. Using three perpendicular lengths defined by the primitive ellipsoid in Blob3D, where L is the longest dimension a particle is fit to, I is the longest dimension perpendicular to L , and S is the dimension perpendicular L and I , equancy is defined as the ratio,

$$\frac{S}{L} = \frac{S}{I} \times \frac{I}{L} = \frac{SI}{IL}$$

where S/I is elongation and I/L is flatness with values ranging from 0 to 1. For elongation and flatness, and equancy there are five classes, 1 – 5 where 1 represents not elongate, not flat and equant and 5 represents extremely elongate, extremely flat and extremely non-equant. Zingg diagrams are used to compare how these particle-form ratios relate to one another. Aspect ratio, L/S , is also calculated for each clast in each series and is described using a Flinn diagram.

To quantify roundness, or the surface roughness, the 3D Convexity, C , is defined by dividing the particle surface area by the convex hull surface area,

$$C = \frac{SA_P}{SA_{CH}}$$

where SA_P is the surface area of the particle output from Blob3D and SA_{CH} is the surface area of an ellipsoid determined by the three perpendicular lengths defined by the primitive ellipsoid in Blob3D. Convexity values range from 0 to 1 (Figure 9).

Sphericity, S , measures how much a particle deviates from a sphere. It is an extension to 2D circularity and is computed from the ratio of volume over surface area.

It is defined as

$$S = \frac{SA_S}{SA_{PE}} = \frac{\pi^{\frac{1}{3}} 6 V_P^{\frac{2}{3}}}{SA_{PE}}$$

Where SA_S is the surface area of a sphere with the same volume as the given particle, V_P is the volume of the particle and SA_P is the surface area of the primitive ellipsoid. The distribution of convexity and sphericity are examined with scatter plots versus particle diameter, and histograms of these shape parameters are recorded.

4. RESULTS

4.1. Classification of Size and Shape

In Blob3D, touching particles are separated using erode and dilate functions or by picking three points to define a plane (Figure 8). The latter introduces a subgroup of particles having a flat side produce by separation along a plane. Additionally, for series F, clasts intersecting the fragment edge are partial clasts produced by splitting during formation of the fragment. For these clasts the size and possibly the shape are artificial, and if they are significant in number the distributions also will be artificial leading to poorly defined probability distributions.

In order to objectively remove artificially shaped or sized clasts and determine the distributions accurately, the couple of hundred largest clasts of each set of data (series A, B, and F) are closely inspected and classified into three categories, where "acceptable" particles are those unaffected by intersection with core or fragment boundaries or separation from connected clasts and retained for size and shape analyses, "useable" particles are those clasts produced by separation from a contact with neighboring particle and are retained for size analysis only, and "excluded" particles are clearly partial clasts produced by intersection with the boundary of the core or fragments and are excluded for both shape and size analysis. The relative number of clasts in the three classes is analyzed in terms of percentage of the cumulative population from largest to increasingly smaller clast size. As logically expected, the very largest clasts are disproportionately classified as excluded. However, after inspecting about 100 of the

largest clasts the relative proportions of the different classes is stable (Figure 10). For series A, 64% of the largest 275 clasts are considered acceptable, 16% are useable, and 20% are excluded. Similarly, for series B, 62% of the largest 282 clasts are considered acceptable, 29% are useable, and 9% are excluded. Likewise, for series F 67 % of the largest 260 clasts are considered acceptable, 17% are useable, and 15% are excluded. For the clasts not inspected, i.e., the clasts smaller than the largest couple hundred, I assume the proportions above are representative, and thus reduce the cumulative number by the fraction of excluded clasts, i.e., the cumulative number for series A, B, and F is incremented by 0.80, 0.91, and 0.85, respectively, for all clasts smaller than the smallest inspected individually.

Cumulative number is normalized by the gouge volume for each dataset. To maintain an accurate volume, the volume sum of all particles excluded in each dataset is subtracted from the gouge volume of each dataset. For each series, the clast shape of only the largest 175 clasts inspected and classified as acceptable are analyzed as described below.

4.2. Distribution of Clasts in the Gouge

Generally, the clasts size is evenly distributed in the SDZ (Figure 11). The three dimensional spatial distribution of the survivor clasts within series A and series B is categorized in to three size ranges, small, medium, and large. I define small to be clasts smaller than 3 mm, medium to be clasts between 3 mm and 5 mm, and large to be clasts larger than 5 mm. For series A, 88% of clasts are small, 9% of clasts are medium, and

3% of clasts are large. For series B, 86% of clasts are small, 11% of clasts are medium, and 3% of clasts are large. Both series appear to be uniformly distributed (Figure 11).

4.3. Clast and Matrix Volume in the Gouge of the SDZ

Percent volume of clasts is also determined for each series. For each dataset, the total clast volume is less than 10% of the volume of the gouge scanned. The clasts from series A make up 2% of the volume of the gouge scanned ($267,174.62 \text{ mm}^3$) and the clasts from series B make up 3% of the volume of the gouge scanned (1496543.14 mm^3). The clasts from series F make up 14% of the volume of the gouge scanned (5833.36 mm^3).

From Series F, I determined the volume percent of clasts larger than the matrix. I first identified the number of clasts smaller than clay/silt size. Using the power law fit with a scaling parameter of 2.99, I extrapolate that there are 1,731,485,009 clasts larger than clay/silt sized grains (0.002 mm). The clasts larger than clay/silt sized grains make up 15% of the volume of gouge sampled from series F (5833.36 mm^3).

4.4. Particle Size Distributions

Particle size distributions of survivor clasts are determined for each series from the SDZ (series A, B, and F). A particle size distribution effect of rejecting clasts from series F is shown in Figure 12 and summarized in Table 4.

The normalized cumulative frequency of each dataset is plotted to illustrate the clast size distribution of each entire scan series less the excluded particle fraction analyzed for lower bound and goodness of fit to the power law using the maximum likelihood estimation and KS statistic [*Clauset et al.*, 2009] (Figure 13). An example of

the general result of the *Clauset et al.* [2009] analysis (Figure 14) is a plot comparing both the original data and lower bound cutoff of series F. The scaling parameter, lower bound, and goodness-of-fit of each dataset are reported in Table 3.

In series A there are 5224 acceptable and useable clasts imaged in the foliated gouge of the SDZ ranging in size from 1 to 13 mm in diameter. The size distribution of the largest 1563 clasts with a lower bound of 2.12 mm is described by a power law with scaling parameter of 3.02. The largest 1563 clasts have a goodness-of-fit of 0.74.

In series B there are 3448 acceptable and useable clasts imaged in the foliated gouge of the SDZ ranging in size from 1 to 15 mm in diameter. The size distribution of the largest 654 clasts with a lower bound of 2.68 mm is best described by a power law with scaling parameter of 3.09. The largest 654 clasts have a goodness-of-fit value of 0.71.

In series F there are 4101 acceptable and useable clasts imaged in the foliated gouge of the SDZ ranging in size from 0.16 to 10 mm in diameter. The size distribution of the largest 1011 clasts with the lower bound of 0.45 mm is best described by a power law with scaling parameter of 2.99. The largest 1011 clasts have a goodness-of-fit value of 0.89.

Additionally, I reanalyzed particle size distributions of survivor clasts from the SDZ and the CDZ using two sets of data from *Sills* [2010]. Clasts from the SDZ and CDZ were imaged at low resolution (512 x 512 pixel resolution) and particle size range from 9.37 to 59.87 mm. Clasts from the CDZ were imaged at high resolution and particle size range from 1.79 to 20.00 mm. These sets of data, referred to as series P and

series U, respectively hereafter. In series U there are 6176 clasts imaged in the foliated gouge of the CDZ ranging in size from 0.67 to 20.00 mm in diameter. The size distribution of the largest 1455 clasts with the lower bound of 1.79 mm is best described by a power law with scaling parameter of 2.83. The largest 1455 clasts have a goodness-of-fit value of 0.84.

In series P there are 278 clasts imaged in the foliated gouge of the SDZ ranging in size from 6.31 to 59.87 mm in diameter. The size distribution of the largest 152 clasts with the lower bound of 9.37 mm is best described by a power law with scaling parameter of 3.13. The largest 152 clasts have a goodness-of-fit value of 0.29. Series A, B, and U are of the same scale range but come from two different creeping segments. A cumulative frequency plot comparing the SDZ (series A and B) with the CDZ (series U) illustrates the scaling parameter is similar (Figure 15). All particle distribution curves in the SDZ are in agreement with similar scaling parameter values of approximately 3 (Figure 16).

4.5. Clast Shape

The shapes of the clasts, as determined from the primitive ellipsoids by Blob3D, are mainly scalene in shape, where all three axes are different. Shapes of the clasts appear to be mostly oblate and sub-equant. The variation in particle form is shown using Flinn diagrams of series A, B, and F with scatter plots of ratios of long to intermediate axis versus intermediate to short axis, and frequency distributions with bin size of 0.25 are plotted (Figure 17). Zingg diagrams of series A, B, and F with scatter plots of elongation versus flatness, and frequency distributions with bin size of 0.1 are also

plotted (Figure 18). A systematic description of particle shape is described in Table 5. The distributions of these particle shape descriptors are summarized in Table 6.

Additionally, Convexity, and sphericity are shown for series A, B, and F as a function of clast size. The variation in particle roughness and sphericity for all clast size is shown with scatter plots of size versus shape descriptor, and with frequency distribution plots with bin size of 0.1 (Figures 19 and 20). Figure 21 shows a sample of clasts used for shape analysis with their corresponding sphericity values. The shape effects of excluded clasts are compared in sphericity plots versus clast size (Figure 22).

The distributions of each shape descriptor, coupling two data sets at a time, are tested using the KS statistic and are summarized in Table 7. The distributions of elongation, sphericity, and aspect ratio are statistically similar with a significance level of 0.01 (99.9% confidence). The distributions of convexity are statistically different for series A with series F and series B with series F. The distributions of flatness are also different for series A with series B and series B with series F.

For series A of the 175 clasts, 83 clasts which fall in to the slightly elongated (Class 2) classification, which makes up 47% of all clasts, while 64 clasts fall in to the not elongated (Class 1) classification, which makes up 37% of all clasts. There are 81 clasts which fall in to the moderately flat (Class 3) classification, which makes up 46% of all clasts, while 67 clasts fall in to the slightly flat (Class 2) classification, which makes up 38 % of all clasts. The equancy ratio of 100 clasts (57%) is between 0.4 and 0.6. For series A, as shown by the Flinn diagram (Figure 17), the majority of clasts (>75%) are more oblate than prolate ellipsoids. The aspect ratio of the majority of the

clasts ($> 75\%$) is between 1.5 and 2.5. As shown by the Zingg diagram (Figure 18), 41% of the clasts are oblate spheroids, 38% of the clasts are sub-equant spheroids, 10% of the clasts are prolate spheroids, and fewer than 10% of the clasts fall into other categories. There are 167 clasts (95%) with convexity values ranging between 0.6 and 1.0. There are 169 clasts (95%) with sphericity values ranging between 0.6 and 1.0.

For series B of the 175 clasts, 89 clasts which fall in to the slightly elongated (Class 2) classification, which makes up 51% of all clasts, while 65 clasts fall in to the not elongated (Class 1) classification, which makes up 37% of all clasts. There are 75 clasts which fall in to the moderately flat (Class 3) classification, which makes up 43% of all clasts, while 68 clasts fall in to the slightly flat (Class 2) classification, which makes up 39 % of all clasts. The equancy ratio of 109 clasts (62%) is between 0.4 and 0.6. For series B, as shown by the Flinn diagram (Figure 17), the majority of clasts ($>71\%$) are more oblate than prolate ellipsoids. The aspect ratio of the majority ($> 78\%$) of all clasts is between 1.5 and 2.5. As shown by the Zingg diagram (Figure 18), 41% of the clasts are oblate spheroids, 41% of the clasts are sub-equant spheroids, 10% of the clasts are prolate spheroids, and fewer than 8% of the clasts fall into other categories. There are 168 clasts (96%) with convexity values ranging between 0.6 and 1.0. There are 170 clasts (97%) with sphericity values ranging between 0.6 and 1.0.

For series F of the 175 clasts, 101 clasts which fall in to the slightly elongated (Class 2) classification, which makes up 58% of all clasts, while 53 clasts fall in to the not elongated (Class 1) classification, which makes up 30% of all clasts. There are 89 clasts which fall in to the slightly flat (Class 2) classification, which makes up 51% of all

clasts, while 68 clasts fall in to the moderately flat (Class 2) classification, which makes up 38 % of all clasts. The equancy ratio of 106 clasts (61%) is between 0.4 and 0.6. For series F, as shown by the Flinn diagram (Figure 17), the majority of clasts (>67%) are more oblate than prolate ellipsoids. The aspect ratio of the majority (> 79%) of all clasts is between 1.5 and 2.5. As shown by the Zingg diagram (Figure 18), 55% of the clasts are sub-equant spheroids, 31% of the clasts are oblate spheroids, and fewer than 14% of the clasts fall into other categories. There are 172 clasts (98%) with convexity values ranging between 0.6 and 1.0. There are 175 clasts (100%) with sphericity values ranging between 0.6 and 1.0.

5. DISCUSSION

5.1. Insights into Deformation Based on Survivor Clast Size

Faulting at several km depth, as documented here in core samples recovered from SAFOD, is characterized by intense and repeated fracture that progressively reduces intact rock into granular material. Confinement at depth restricts the ability of particles to move freely, in which case the likelihood of particle fracture and further particle refinement is highly dependent on loading by the nearest neighboring particles. In this case, the greatest probability for a particle to fracture is when it is in contact and loaded by similar sized particle [Sammis *et al.*, 1987, Sammis & King, 2007]. Models for comminution identify the probability of a particle fracture to determine the size distribution of particles that are produced. Nearest neighbor fragmentation models have been successful in explaining observed particle size distributions for granular material in fault zones.

In the case of the constrained comminution model, which may be most appropriate for low strain zones, individual particles break in to smaller fragments of similar size and progressive fracturing leads to refinement but retention of some larger particles. This model of comminution predicts a power law scaling with a 3D mass- or volume-dimension of 2.58 [Sammis *et al.*, 1987]. As the cumulative strain increases, and the magnitude of shear increases, the particle size in the shear zone continues to decrease, resulting in fewer large clasts [Blenkinsop, 1991]; consequently, it may appear that the scaling parameter increases, particularly for the upper range of particle sizes.

In the case of high strain fault gouge, particles move with respect to nearest neighbors as a result of shear strain. In this case same-size particles are isolated, but come into contact depending on the number of similar-sized particles within the shearing volume. *Sammis & King* [2007] show that the only for a power law distribution with 3D mass dimension of 3.0 is the probability for same-size particles to come in contact independent of particle size.

In high strain zones other processes can lead to particle size reduction. For example, abrasion of particles from frictional sliding and wear can progressively reduce particle size. Similarly, mineral reactions and dissolution along the surfaces of particles, which would likely depend on mechanical and chemical processes can lead to reduction in size. Some workers have these processes are possibly indicated by the presence of tapered and elongated clasts in natural and experimental shear zones [*Bos and Spiers*, 2001; *Sills*, 2010; *Moore & Rymer*, 2012]. Models of size distributions by these additional processes are not currently developed.

Currently, particle size distributions of fault rocks determined through a variety of measurement techniques, mostly in 2D, are found to be approximately fit by power law relations, and the observed distributions are often represented by the slope of the best fit line on a log-log plot of particle size versus cumulative number or frequency. While this approach provides a means of generalizing particle size data, there has been little work in statistically robust and effective methods for determining the range of particles fitting a power law distribution. Although power law distributions arising from natural processes are expected to have physically-based limits that reflect the process or

scale of operation, *Bonnet et al.* [2001] addresses two other issues associated with observations of natural power-law distributions over a large range of scale, specifically the upper and lower cutoff in particle size, as reflected by apparent deviations in the power law fit to natural distributions, caused by the censoring and truncation effect. In the context of particle size distributions, censoring describes deviation at the upper size limit bounded by the largest particle that is wholly contained within the sampled volume. While truncation describes deviation at the lower particle size limit bounded at the smallest particle that can be resolved at the scale of observation, i.e., effectively the point at which the smallest particle captured in a volume is limited by the set resolution of the image. The censoring effect greatly affects the data sampling at the upper size limits, and can produce unpredictable deviations in over- or under-predicting the true population. The truncation effect greatly affects the data sampling of smaller particles because the roll-off on a log-log plot shows undercounting of smaller particles. Both of these effects can be seen in the raw data sets of individual series herein, The likelihood of censoring effects seen in the roll-off at small particle sizes in series A and series B was one of the motivations to create a fabricated sample, series F, and observe an order of magnitude smaller sized clasts.

In the SDZ, by combining series A, B, F, and P, clast size is scale invariant over the range of clasts from 0.45 mm to 60 mm, with a power law scaling parameter of 3. Following the statistical method of *Clauset et al.* [2009] I tested the goodness-of-fit of the scaling parameter and compare my value to published model predictions. All of the

tested datasets fit a power law distribution ($p > .01$), so there is no need to test if any other distribution provide a better fit.

The observed homogenous distribution of small volume of clasts relative to the volume of very fine matrix in the SDZ gouge layers implies clasts of any size infrequently come in to contact, much less clasts of similar size. Three-dimensional rendering of clasts within the imaged volumes agree with the expectation as only a small percentage of clasts are in contact, and similar sized clasts in contact make up an even smaller fraction. Since the clasts entirely supported by fine-grained matrix, and the clasts are uniformly distributed, and clasts are not constrained by nearest neighbors. Survivor clasts uniform distribution result in infrequent contact between similar sized particles, which supports the inherent assumptions of the nearest neighbor fragmentation model for large shear strain posed by *Sammis and King* [2007]. For this model, a power law scaling parameter of 3 is the posed theoretical limit for high strain shear zones as observed for the gouge clasts. The determined scaling parameter of 3 for the survivor clasts is consistent with the model prediction of 3.0. The survivor clasts from the CDZ also fit a power law distribution with scaling parameter of 3.

5.2. Insights into Deformation Based on Survivor Clast Shape

Few fault rock studies quantify particle shape as a means to infer kinematic and deformation mechanisms [*Mair et al.*, 2002; *Storti et al.*, 2003; *Heilbronner & Keulen*, 2006; *Bjork et al.*, 2009]. *Mair et al.* [2002] discovered kinematic differences between numerically simulated spherical grains and angular grains produced in laboratory experiments. *Mair et al.* [2002] determined that gouge with spherical particles is weaker

than gouge with angular particles; however, aside from these end members, very little has been done to explore particle shape in three-dimensions.

In the case of the survivor clasts in the gouge of the SDZ, the inferred clast fragmentation process would be by fracture extension causing clasts to split so as to produce hemispherical objects or objects displaying a flat-sided area. In general, clasts with hemispherical shapes are not commonly observed in the imaged samples; thus, another deformation process may be operating in shaping of the clasts.

There is no strong evidence that roughness (based on convexity values) changes with respect to clast shape; shape distributions of sphericity, elongation and aspect ratio all indicate that shapes of clasts are scale invariant over the scale range of 0.72 mm to 13.40 mm in diameter. The high sphericity values of survivor clasts herein is inconsistent with clast shape resulting from fragmentation only. *Bjork* [2009] suggests abrasion processes dominate the granular shape of material from a clastic dike from the Hornelen basin through their characterization of circularity (similar to sphericity) and convexity analysis. Lenticular shaped survivor clasts both experimental [*Bos and Spier*, 2001] and natural [*Sills*, 2010] may be a signature shape indicative of pressure solution. *Bos and Spier* [2001] found frictional wear processes to be dominant in their experiments where frictional and time dependent chemical alteration processes would be operating. However, based on the shapes of the halite porphyroclasts in the later stages of the experiment they suggest pressure solution to be a contributing mechanism active in the shaping process. Analysis of SDZ clast shapes herein suggests the clast morphology could be the result of surface wear processes either by abrasion, pressure

solution, or a combination effect of both processes; but, the observations of shape alone cannot discriminate between abrasion and pressure solution.

5.3. Quasi Steady-state Condition

The low volume of clasts to foliated gouge and uniform distribution of clasts across the gouge implies that the survivor clasts are entirely matrix supported in the SDZ within the gouge. A globally steady state condition for clasts in the gouge implies replenishment of large clasts and continued fracturing to produce smaller clasts eventually contributing to the matrix. Size distribution of survivor clasts in SDZ and CDZ are scale invariant and similar; this suggests both deforming zones are formed under similar conditions, and are likely experiencing the same deformation mechanisms. My findings are consistent with conclusions of *Sills* [2010] that the evolution of the structure of the gouge, specifically the survivor clasts, from SDZ and CDZ has developed through time to a quasi steady state condition.

5.4. Similarities in the SDZ and CDZ

Survivor clasts from the CDZ are scalene in shape and the majority of clasts are oblate ellipsoids [*Sills*, 2010]. This is in agreement with shape analysis herein of survivor clasts from the SDZ. *Sills* [2010] hypothesized that clast size reduction is caused by mechanical and chemical surface-shaping processes rather than intraclast fracture or flow. Similarities in survivor clast size suggest both gouge zones undergo the same processes. The findings of homogenous deformation across both gouge zones support aseismic creep associated with distributed flow. Similarities in clast size distributions, consistency with the high-strain fragmentation model, shape of survivor

clasts, and conclusions made from the orientation distribution of clasts [*Sills*, 2010], lead to the hypothesis that clast size distributions reflect nearest neighbor fracture as the dominant process in clast size reduction, but that the dominant shaping mechanism in the SDZ is the result of surface wear processes such as abrasion or pressure solution.

With clast size reduction, pressure solution can become increasingly important. However, scale invariance of the clast size suggests it is not the dominating deformation mechanism associated with the actively creeping deforming zones, at least at the scale of observation to date; rather brittle processes likely dominate these deforming zones. Future work should include size and shape analysis of even finer particle sizes to better assess the role of mineral reactions and dissolution processes in the gouge.

6. CONCLUSIONS

6.1. Findings

The key findings from this research are:

- Employing the statistical method of *Clauset et al.* [2009], which provides a robust method to determine whether the particle size distribution is consistent with a power law, identify the lower bound to avoid bias from the truncation effect, and determine the scaling parameter with confidence, indicates the particle size distributions of survivor clasts from the SDZ and CDZ fit a power-law scaling relation.
- Size distribution of survivor clasts in the SDZ and CDZ are scale invariant and similar; spatial distribution of clasts suggests that the gouge layers have attained a mature, quasi steady state condition.
- Particle size analysis suggests that the reduction in the size of clasts is a result of brittle fragmentation processes. The scaling parameter is consistent with a nearest neighbor fragmentation model for a high strain shear zone.
- Particle shapes are characterized by as oblate spheroids, moderate (1.5-2.5) aspect ratio with high convexity and sphericity (>0.6), and appear invariant with clast size. The high convexity and sphericity of the clasts is likely a result of surface wear processes such as abrasion or pressure solution.

6.2. Conclusions

The main conclusions from this research are:

- Size-frequency distribution of survivor clasts is scale invariant down to 0.45 mm size and implies that the aseismic creep is accommodated by flow processes operating in the gouge matrix at a smaller scale much smaller than the smallest clasts measured herein.
- Analysis of particle size distribution should be combined with shape analysis to better constrain comminution processes within gouge and other fault rocks.
- The documented size and shape characteristics in the clasts of the SAFOD gouge may be diagnostic of aseismic creeping flow in fault but this demands comparative studies with other known creeping and seismic fault zones.

REFERENCES

- An, L. J. and C. G. Sammis (1994), Particle size distribution of cataclastic fault materials from Southern California: A 3-D study, *Pure and Applied Geophysics*, 143(1-3), 203-227.
- Bjørk, T. E., K. Mair, and H. Austrheim (2009), Quantifying granular material and deformation: Advantages of combining grain size, shape, and mineral phase recognition analysis, *Journal of Structural Geology*, 31(7), 637-653, doi:10.1016/j.jsg.2009.03.020.
- Blenkinsop, T. G. (1991), Cataclasis and processes of particle size reduction, *Pure and Applied Geophysics*, 136(1), 59-86.
- Blott, S. J. and K. Pye (2008), Particle shape: a review and new methods of characterization and classification, *Sedimentology*, 55(1), 31-63, doi:10.1111/j.1365-3091:2007.00892.x.
- Bonnet, E., O. Bour, N. E. Odling, P. Davy, I. Main, P. Cowie, and B. Berkowitz (2001), Scaling of fracture systems in geological media, *Reviews of Geophysics*, 39(3), 347-383.
- Bos, B., and C.J. Spiers, (2001), Experimental investigation into the microstructural and mechanical evolution of phyllosilicate-bearing fault rock under conditions favouring pressure solution, *Journal of Structural Geology*, 23(8), 1187-1202.

- Chester, J.S., Chester, F.M., Kirschner, D., Evans, J.P., Sills, D.W., and Coble, C.G., (2008), Structure of the San Andreas Fault Zone at SAFOD, *Geol. Soc. Am. Abstr. Prog.*, v. 40, n. 6, Abstract 147-5.
- Clauset, A., C. R., Shalizi, and M. E. J., Newman (2009), Power-law distributions in empirical data, *SIAM Review* 51(4), 661-703.
- Crompton, C. (2005), Particle shape, an important parameter in pharmaceutical manufacturing, *Pharmaceutical Manufacturing and Packing Sourcer, Samedan Ltd.*
- Heilbronner, R., and N. Keulen (2006), Grain size and grain shape analysis of fault rocks, *Tectonophysics*, 427(1), 199-216, doi:10.1016/j.tect.2006.05.020.
- Heron, B. (2011), Grain-scale comminution and alteration of Arkosic rocks in the damage zone of the San Andreas Fault at SAFOD, Master's thesis, Texas A&M University, College Station, TX.
- Holdsworth, R.E., E. W. E. van Diggelen, C. J., Spiers, J. H. P. de Bresser, R. J. Walker, and L. Bowen (2011), Fault rocks from the SAFOD core samples: implications for weakening at shallow depths along the San Andreas Fault, California, *Journal of Structural Geology*, 33(2), 132-144.
- Ketcham, R. A. (2005), Computational methods for quantitative analysis of three-dimensional features in geological specimens. *Geosphere*, 1(1), 32-41.
- Lockner, D. A., C. Morrow, D. Moore, and S. Hickman (2011), Low strength of deep San Andreas fault gouge from SAFOD core, *Nature Letter*, 472(7341), 82-85.
- Mair, K., K. M. Frye, and C. Marone (2002), Influence of grain characteristics on the

- friction of granular shear zones, *Journal of Geophysical Research*, 107(B10), 2219, doi:10.1029/2001JB000516.
- Marone, C., and C. H. Scholz (1989), Particle-size distribution and microstructures within simulated fault gouge, *Journal of Structural Geology*, 11(7), 799-814.
- Mei, S., and D. L. Kohlstedt (2000a), Influence of water on plastic deformation of olivine aggregates 1. Diffusion creep regime, *Journal of Geophysical Research*, 105(B9), 21457-21469.
- Mei, S., and D. L. Kohlstedt (2000b), Influence of water on plastic deformation of olivine aggregates 2. Dislocation creep regime, *Journal of Geophysical Research*, 105(B9), 21471-21481.
- Mittempergher, S., G. D. Toro, J. P. Gratier, J. Hadizadeh, S. A. F. Smith, and R. Spiess, (2011), Evidence of transient increases of fluid pressure in SAFOD phase III cores, *Geophysical Research Letters* 38(3), doi:10.1029/2010GL046129.
- Moore, D. E., and D. A. Lockner (2013), Chemical controls on fault behavior: Weakening of serpentinite sheared against quartz-bearing rocks and its significance for fault creep in the San Andreas system, *Journal of Geophysical Research-Solid Earth*, 118(5), 2558-2570, doi:10.1002/jgrb.50140.
- Moore, D. E., and M. J. Rymer (2007), Talc-bearing serpentinite and the creeping section of the San Andreas fault, *Nature*, 448(7155), 795-797.
- Moore, D. E. and M. J. Rymer (2012), Correlation of clayey gouge in a surface exposure of serpentinite in the San Andreas Fault with gouge from the San Andreas Fault Observatory at Depth (SAFOD), *Journal of Structural Geology*, 38, 51-60.

- Sammis, C., G. King, and R. Biegel (1987), The kinematics of gouge deformation, *Pure and Applied Geophysics*, 125(5), 777-812.
- Sammis, C. G., and G. C. P. King (2007), Mechanical origin of power law scaling in fault zone rock, *Geophysical Research Letters*, 34(4), doi:10.1029/2006gl028548.
- Sibson, R. H., (1973), Interactions between temperature and pore-fluid pressure during earthquake faulting and a mechanism for partial or total stress relief, *Nature* 243(126), 66-68, doi:10.1038/physci243066a0.
- Sibson, R. H., (1977), Fault rocks and fault mechanisms, *Journal of Geophysical Society* 133(3), 191-213.
- Sibson, R. H. (1986), Brecciation processes in fault zones: inferences from earthquake rupturing, *Pure and Applied Geophysics*, 124(1-2), 159-175.
- Sills, D. W., (2010), The fabric of clasts, veins and foliations within the actively creeping zones of the San Andreas Fault at SAFOD: implications for deformation processes, Master's thesis, Texas A&M University, College Station, TX..
- Storti, F., A. Billi, and F. Salvini (2003), Particle size distributions in natural carbonate fault rocks: insights for non-self-similar cataclasis, *Earth and Planetary Science Letters*, 206(1), 173-186.
- Titus, S. J., C. DeMets, and B. Tikoff (2006), Thirty-five-year creep rates for the creeping segment of the San Andreas Fault and the effects of the 2004 Parkfield earthquake: constraints from alignment arrays, continuous global positioning system, and creepmeters, *Bulletin of the Seismological Society of America*,

96(4B), S250-S268.

Wu, F. T., (1978), Mineralogy and physical nature of clay gouge, *Pure Applied Geophysics*, 116(4-5), 655-689.

Zoback, M., S. Hickman, W. Ellsworth, and the SAFOD Science Team (2011), Scientific drilling into the San Andreas Fault zone—an overview of SAFOD's first five years, *Scientific Drilling*, 11, 14-28.

APPENDIX A
FIGURES AND TABLES

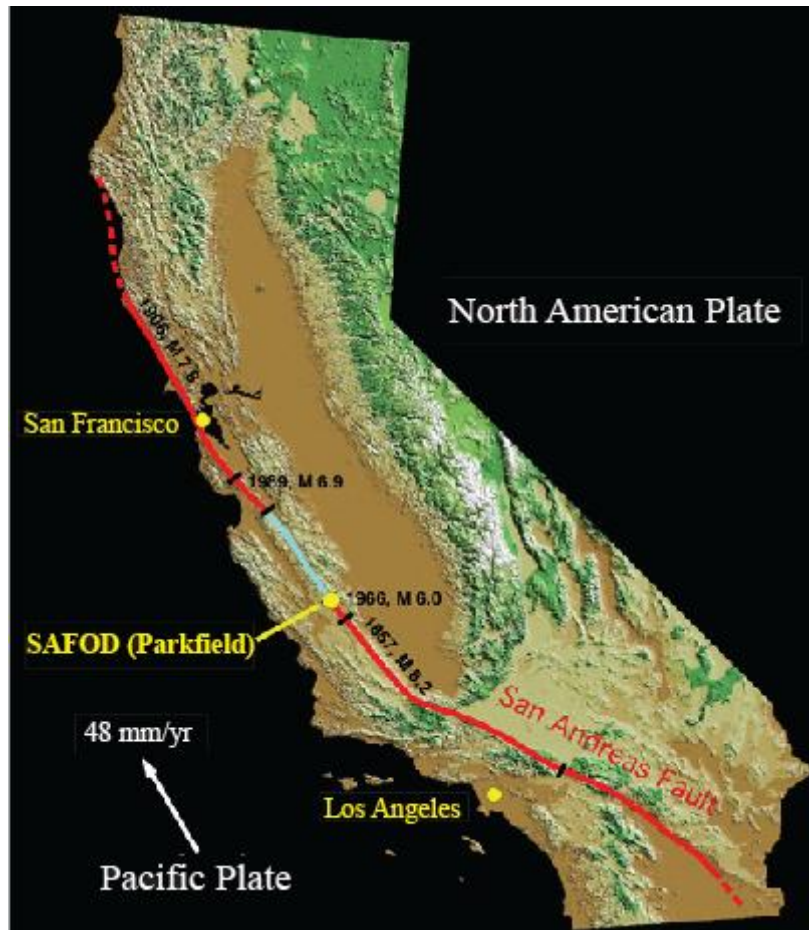


Figure 1. Map of California showing the locations of SAFOD, the creeping section (green), and locked sections (red) of the San Andreas Fault, a continental transform fault that has accommodated hundreds of kilometers of relative motion between the North American Plate and the Pacific Plate.

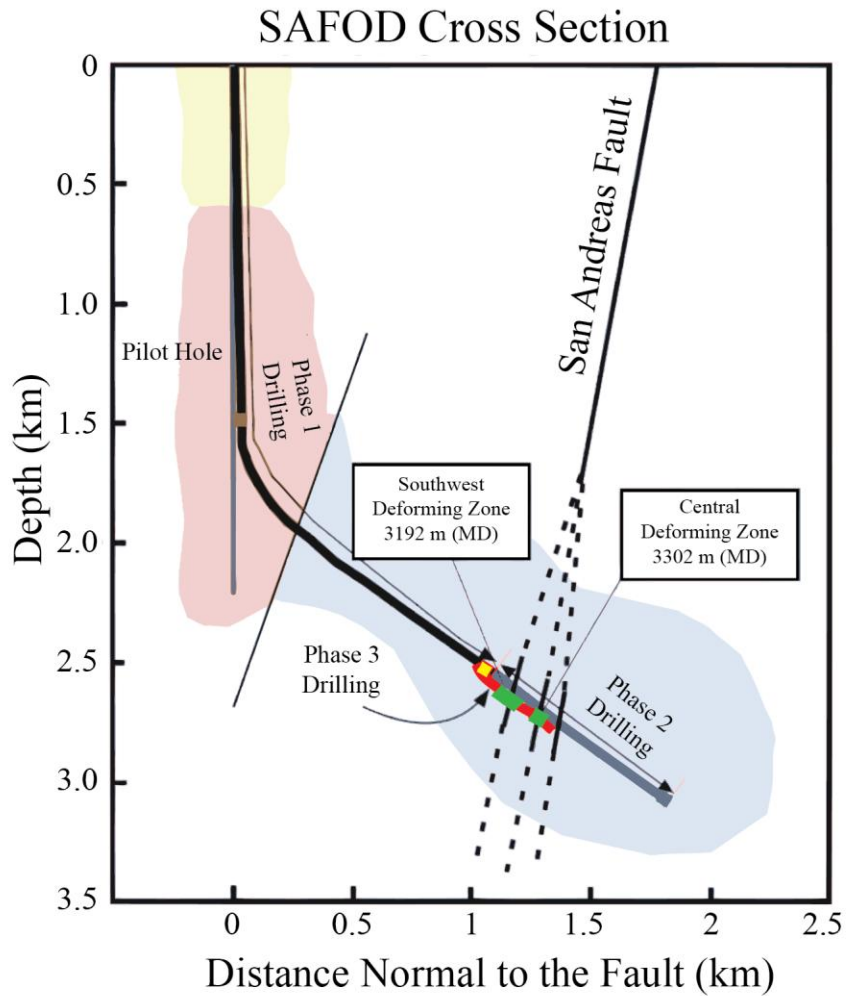


Figure 2. A cross section illustrating the SAFOD borehole geometry and identifying the three phases of drilling [modified from Chester et al., 2008 and Sills, 2010]. The core that was XCT scanned at high resolution, and the fabricated sample scanned at even higher resolution was taken from the foliated gouge zone of the creeping SDZ, which was retrieved during Phase 3 sidetrack drilling.

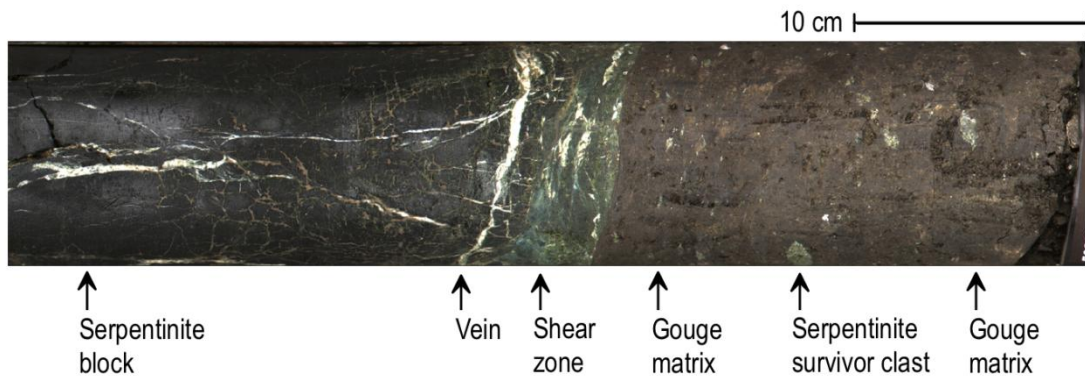


Figure 3. Photographic image of the surface of a portion of the G2S7 core from the SDZ that was scanned for this study [modified from J. S. Chester].

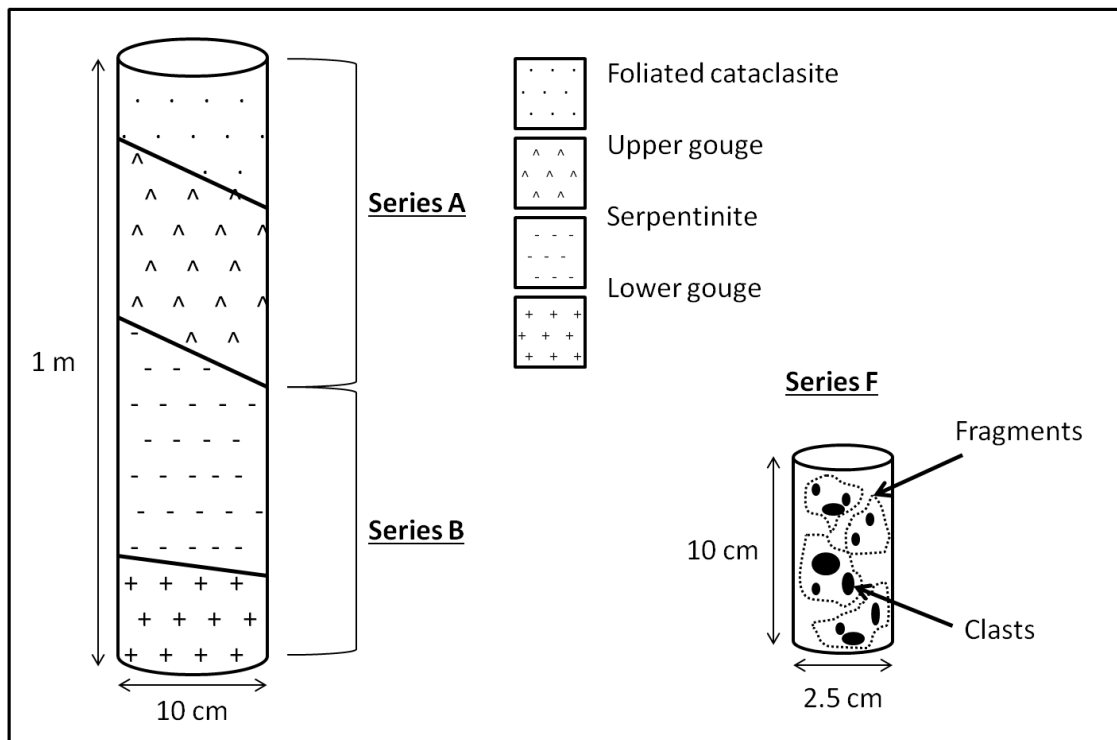


Figure 4. Schematic diagram showing the dimensions and composition of the cores scanned by XCT in scan series A, B, and F. The focus of this research is on the survivor clasts from the upper gouge imaged in scan series A, the survivor clasts from the lower gouge imaged in scan series B, and the survivor clasts within the fragments of gouge in the fabricated core imaged in scan series F.

Table 1. XCT Images (slices) covering units of SDZ G2S7 core for series A and B.

Slice #	Material
a0001-0204	Foliated cataclasite
a0205-0465	Contact between foliated cataclasite and upper gouge
a0466-0767	Upper gouge
a0768-1008	Contact between upper gouge and serpentinite
a1009-1055	Serpentinite
b0001-0350	Serpentinite shear zone
b0351-0520	Contact between serpentinite shear zone and lower gouge
b0521-0538	Serpentinite shear zone
b0539-0571	Contact between serpentinite shear zone and lower gouge
b0572-0944	Lower gouge

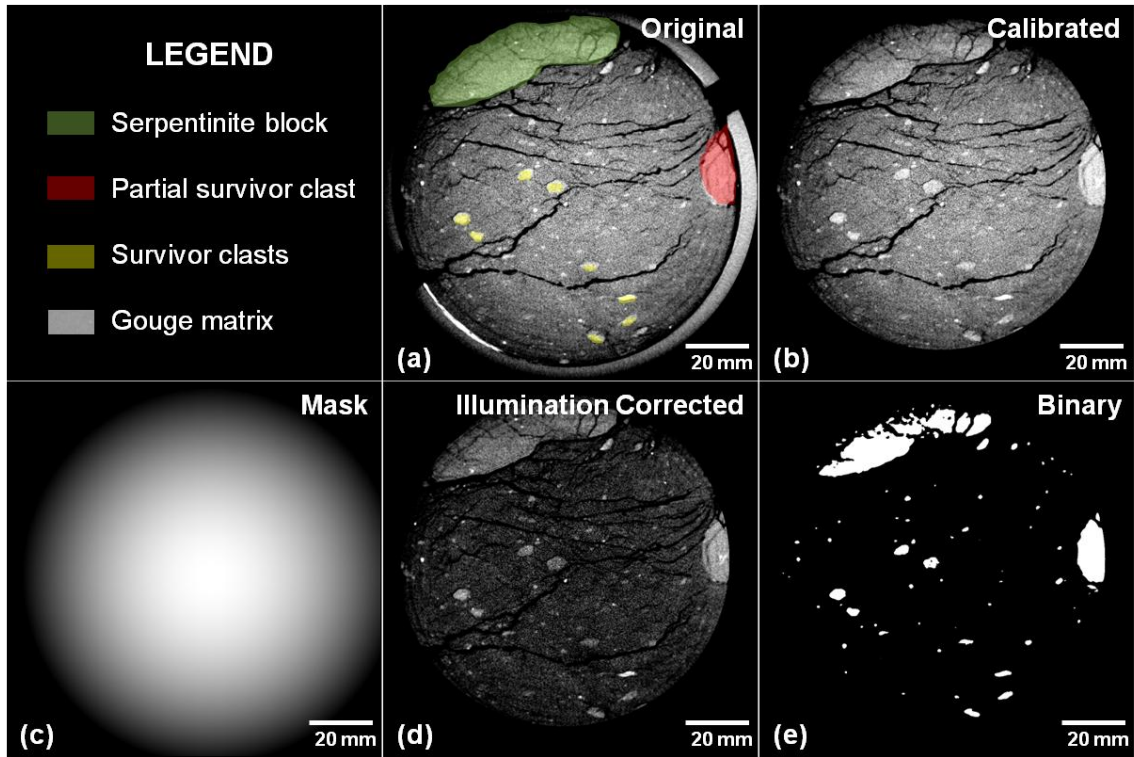


Figure 5. Collection of XCT images illustrating image processing techniques applied to scan series A and B images using code written in Matlab. Images (a) through (e) are of slice number 600 from series A. (a) The original XCT image highlighted by color showing specific gouge and clast components including a serpentine block, partial survivor clast, survivor clasts, and gouge matrix. (b) The XCT image (a) after density calibration and with the aluminum sleeve removed. (c) The mask created to correct uneven illumination in (a) and (b). (d) The XCT calibrated image after the mask has been applied to (b) showing uniform illumination. (e) The XCT binary image produced by thresholding (d) so the matrix is black and the survivor clasts are white.

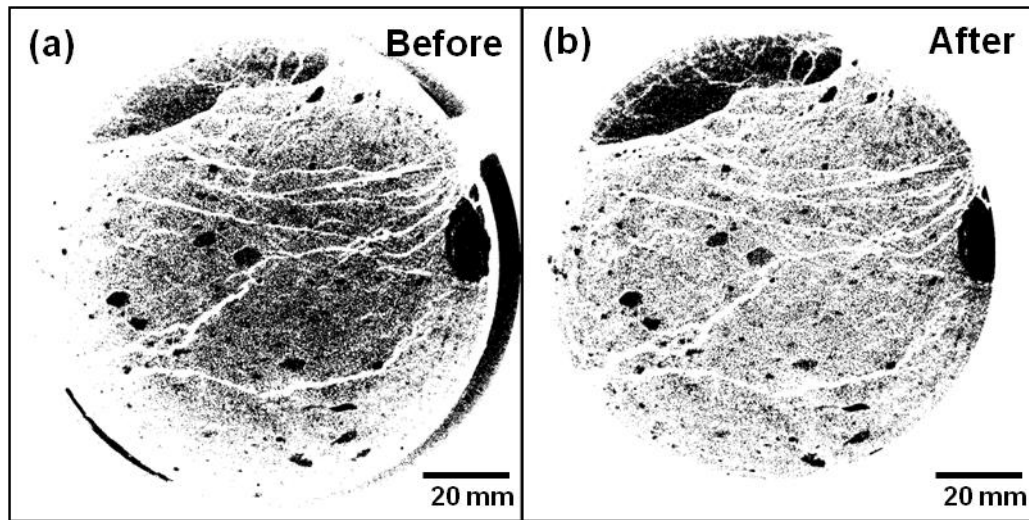


Figure 6. Set of XCT images showing the effects of image processing techniques applied to series A and B. Images (a) and (b) are of slice number 600 from series A. (a) Original XCT image with uneven illumination. (b) Calibrated image after mask has been applied to correct uneven illumination.

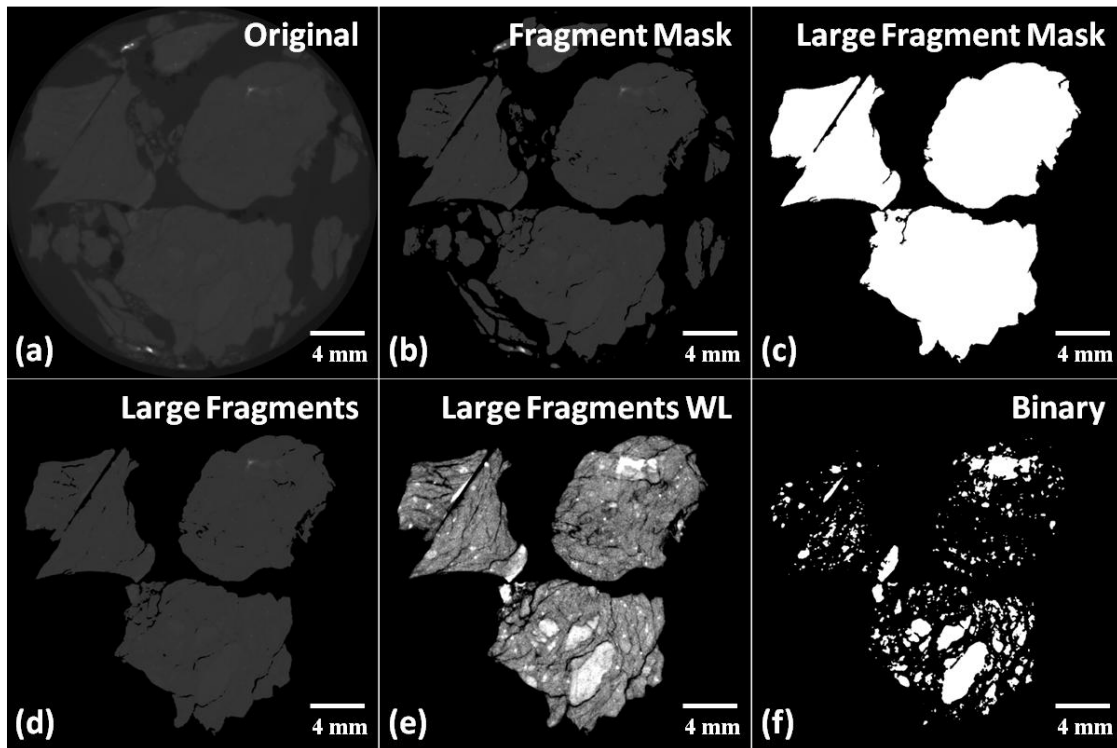


Figure 7. Collection of XCT scans illustrating image processing techniques applied to series F using code written in Matlab. Images (a) through (f) are of slice number 500 from series F. (a) The original XCT image. (b) The calibrated XCT image of fragments with epoxy removed. (c) The large fragment mask used to remove small fragments. (d) The XCT calibrated image after the mask has been applied. (e) The same image from (d) with an adjusted window and level to make clasts visible. (f) The XCT binary image produced by thresholding (e) so the matrix is black and the survivor clasts are white

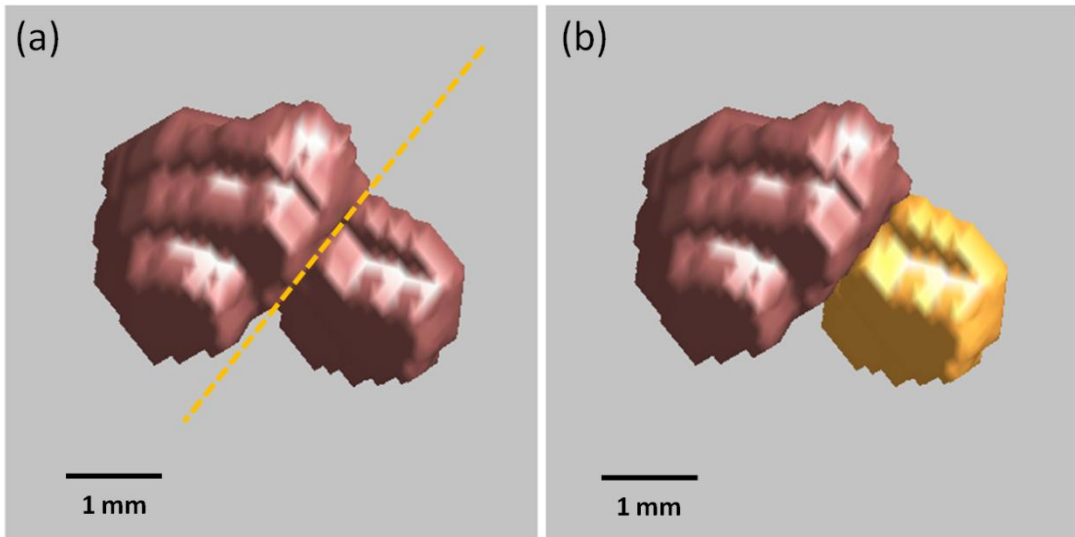


Figure 8. A 3D reconstructed blob showing two joined clasts that must be manually separated prior to size analysis. (a) Two clasts that are touching and connected in the blob showing the user defined (by picking three points) plane of separation (dashed yellow line). (b) The two touching clasts (distinguished by color) after separation of the blob.

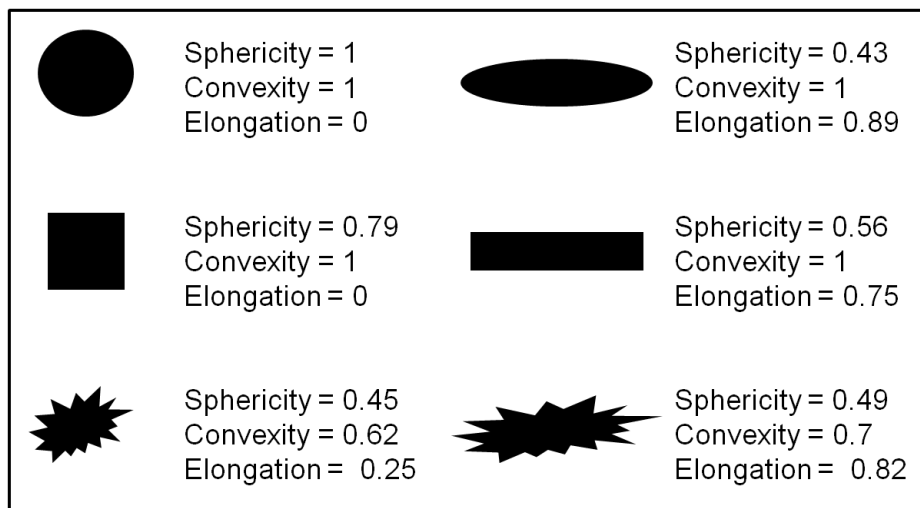


Figure 9. Example values of sphericity, convexity, and elongation for different 2D particle shapes. Sphericity describes how much a particle deviates from a sphere, convexity describes the surface roughness of a particle, and elongation describes the overall form of a particle, independent of roughness. [modified from *Crompton, 2005* and *Heron, 2011*].

Table 2. Blob3D Input parameters used for 3D reconstruction of clasts.

Data Set	Inter-pixel spacing (mm)	Inter-slice spacing (mm)	Upper bound (mm)	Lower bound (mm)	Minimum voxel
series A	0.116	0.45	13.45	1.09	165
series B	0.116	0.45	14.5	1.24	165
series F	0.02892	0.026	2.4957	0.1554	165

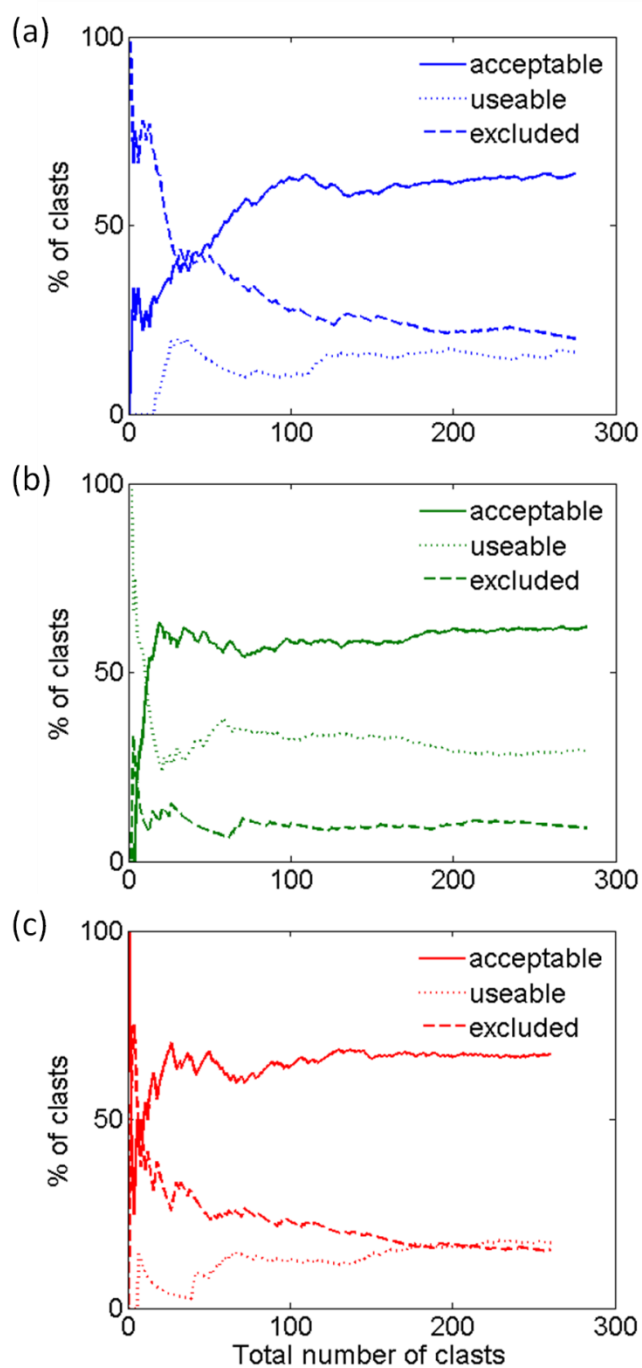


Figure 10. Distribution of acceptable, useable, and excluded clasts for particle size and shape quality classification as a function of cumulative number of clasts analyzed starting with the largest clast. (a) Distribution for the largest 275 clasts of scan series A. (b) Distribution for the largest 282 clasts of scan series B. (c) Distribution for the largest 260 clasts of scan series F.

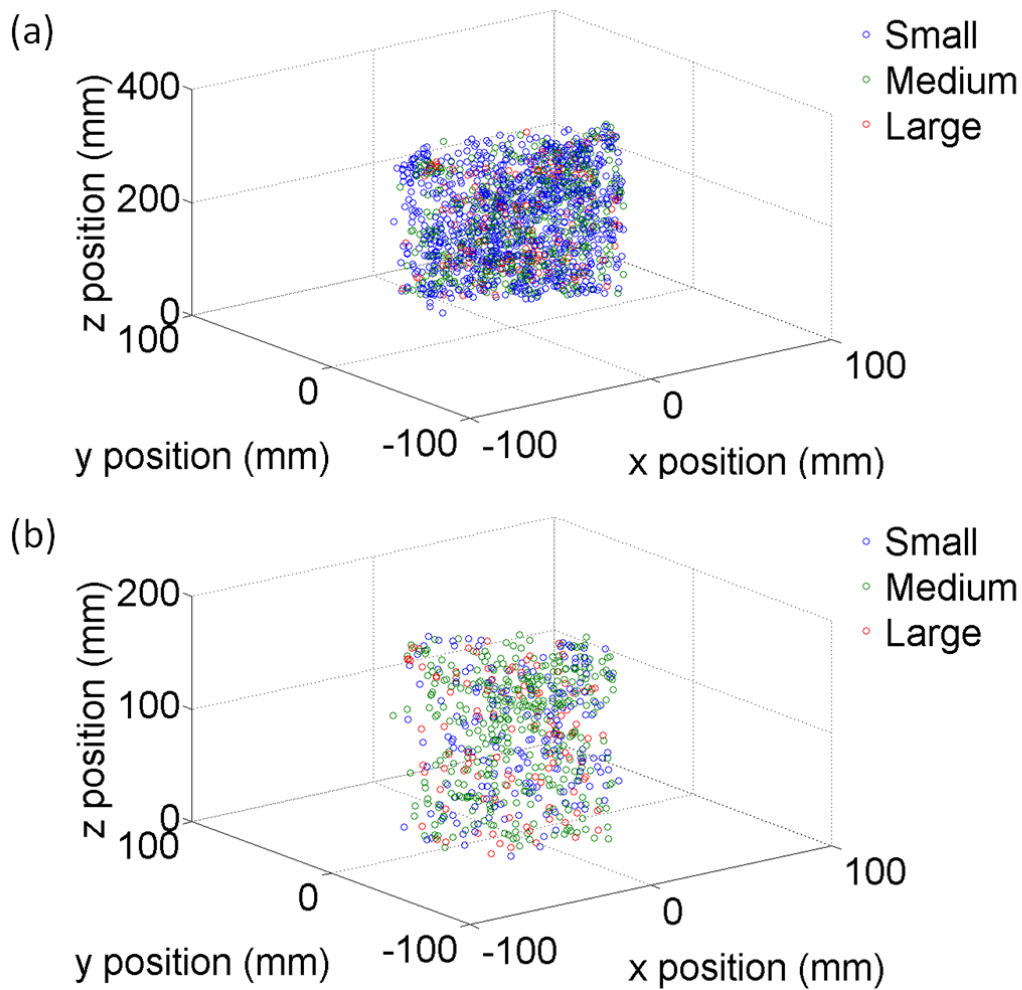


Figure 11. Spatial distribution of clasts within the foliated gouge in the SDZ as a function of clast-size range. Clast size is defined as the equivalent spherical diameter where small refers to clasts smaller than 3 mm, medium refers to clasts between 3 and 5 mm, and large refers to clasts larger than 5 mm. (a) Spatial distribution of clasts within scan series A. (b) Spatial distribution of clasts within scan series B.

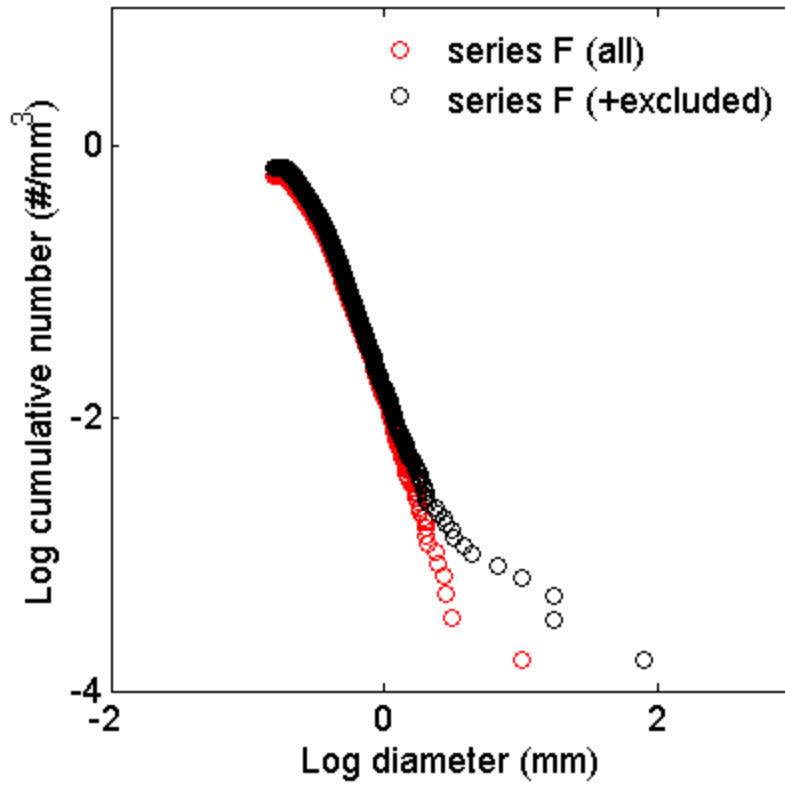


Figure 12. Particle size distribution of clasts within the scan series F of the SDZ comparing data sets with and without the excluded clasts. Series F (all) refers to all the clasts used for particle size analysis (acceptable and useable). Series F (+excluded) refers to all the clasts including excluded clasts (acceptable, useable, and excluded). Cumulative frequency is normalized by the total volume of the fault gouge contained within the fragments from series F.

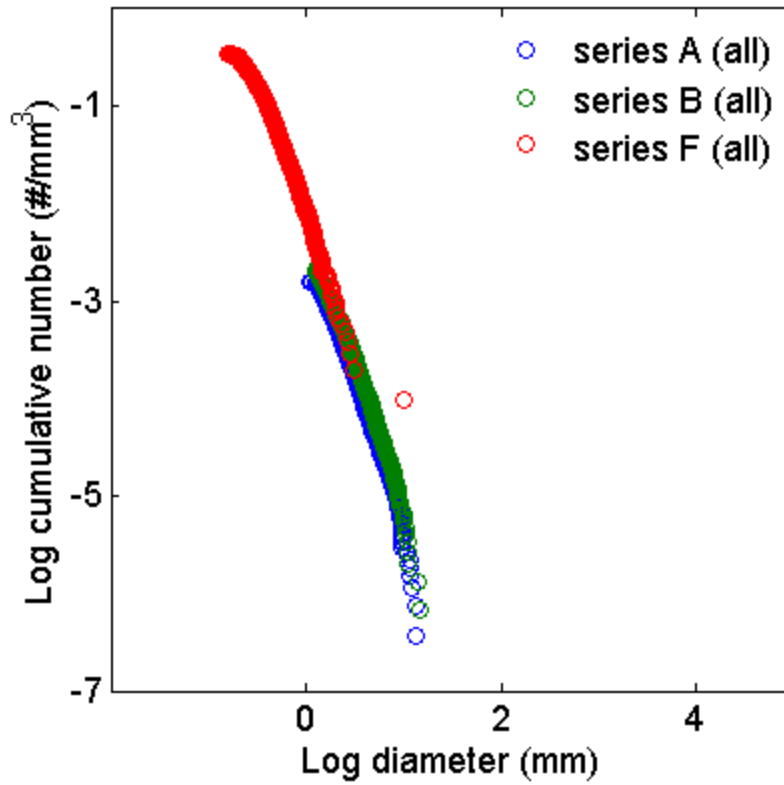


Figure 13. Particle size distribution for clasts within the SDZ at two scale ranges. All refers to all the clasts used for particle size analysis (acceptable and useable). Series A clast sizes range from 1.09 mm to 13.45 mm, series B clast sizes range from 1.24 mm to 14.50 mm, and series F clast sizes range from 0.15 mm to 10.03 mm. Cumulative frequency is normalized by the total volume of fault gouge scanned in each series.

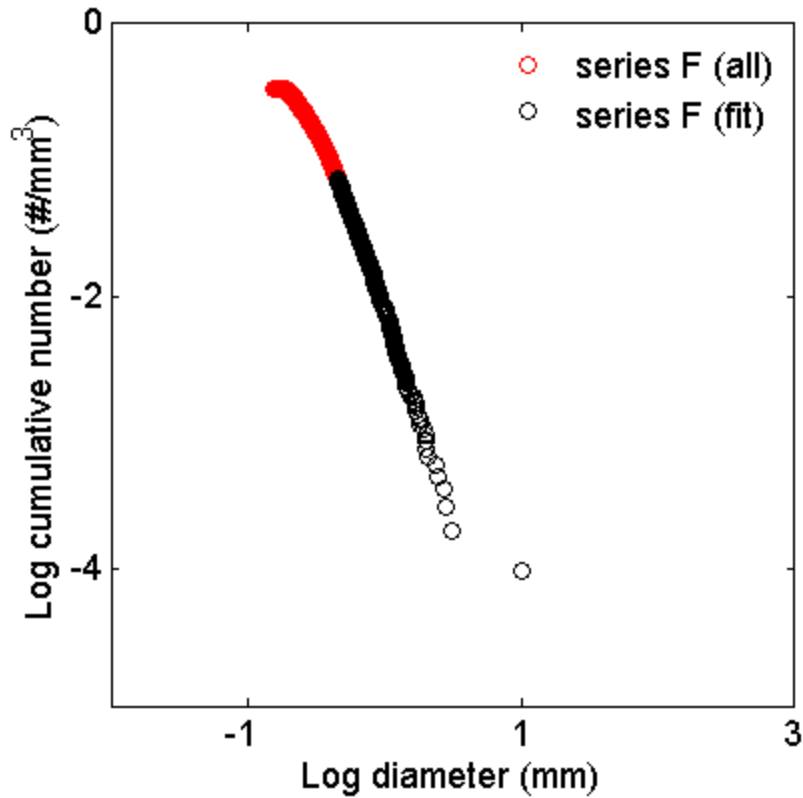


Figure 14. Particle size distribution for clasts within the SDZ from scan series F showing the portion of the data set that fits a power law distribution based on the method of *Clauset et al.* [2009]. All refers to all the clasts used for particle size analysis (acceptable and useable). The scan series F clast-sizes range from 0.15 mm to 10.03 mm. Fit refers to all the clasts larger than the lower bound cutoff that fit a power law distribution. Fit series F clasts range from 0.45 mm to 10.03 mm. Cumulative frequency is normalized by the total volume of the fault gouge contained within the fragments from series F.

Table 3. Particle size distribution results.

Data Set	Volume of fault gouge (mm ³)	Upper bound (mm)	Lower bound (mm)	Power Law scaling parameter (n)	Goodness of fit (p)
SDZ series A	2671742	13.45	2.16	2.81	0.53
SDZ series B	1496543	14.50	2.68	2.99	0.54
SDZ series F	5833	10.03	0.45	2.99	0.89
CDZ series U	1621463	20.00	1.79	2.83	0.84
SDZ series P	18225254	59.87	9.37	3.13	0.29

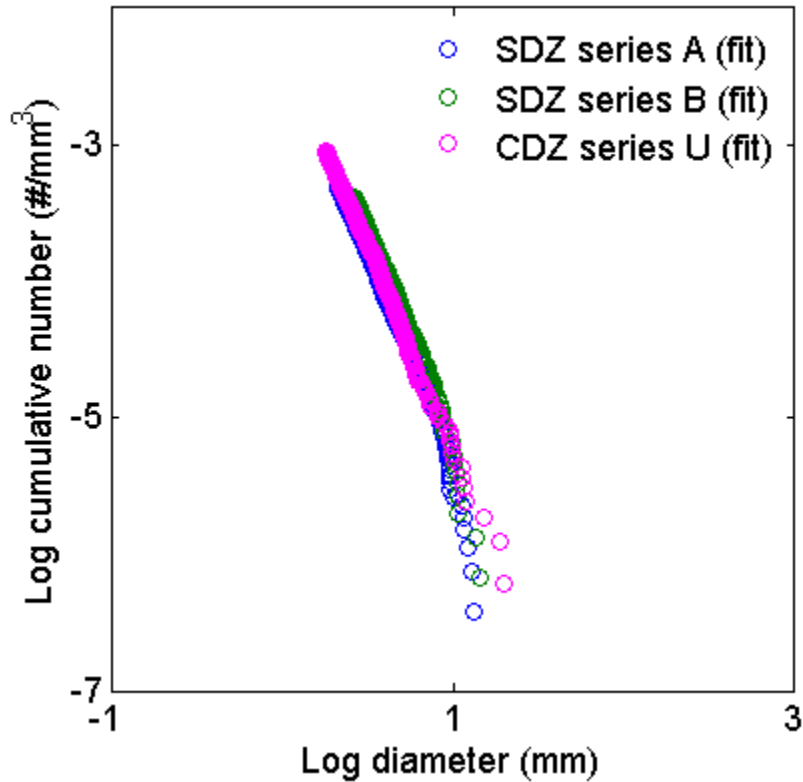


Figure 15. Particle size distribution plot for survivor clasts within the SDZ and CDZ over the same scale range. Fit refers to all the clasts larger than the lower bound cutoff that fit a power law distribution as determined using the method of *Clauset et al.* [2009]. Scan series A clasts range from 2.16 mm to 13.45 mm, series B clast sizes range from 2.68 mm to 14.50 mm, and series U clast sizes range from 1.79 mm to 20.00 mm. The power law scaling parameter for each series is 2.81, 2.99, and 2.83 respectively. Cumulative frequency is normalized by the total volume of fault gouge scanned in each series. The CDZ series U, with permission, is particle size data collected by *Sills* [2010] imaged using the same high resolution UTCT facility as the SDZ herein.

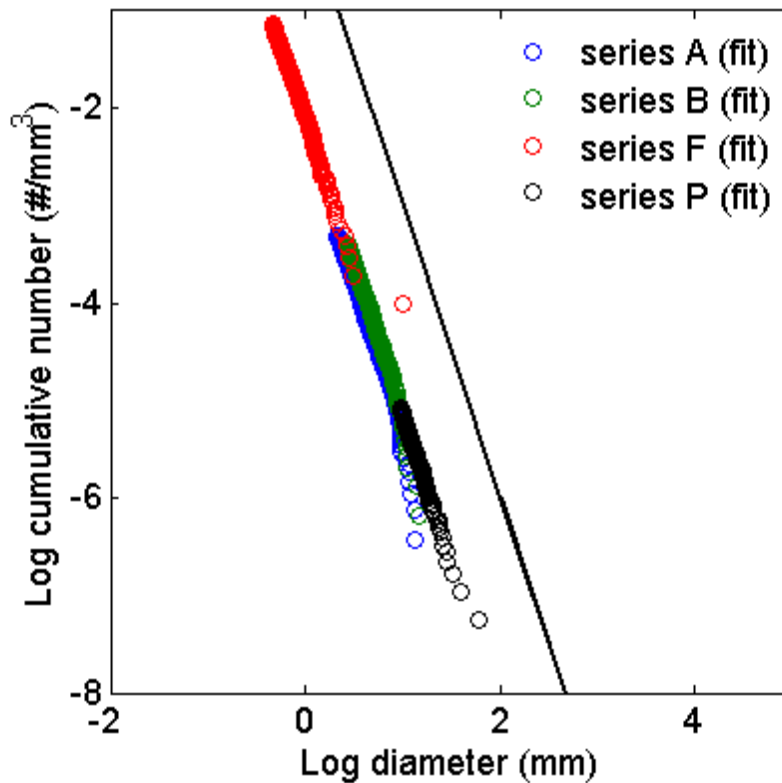


Figure 16. Composite particle size distribution plot for survivor clasts within the SDZ over three scale ranges. Fit refers to all the clasts larger than the lower bound cutoff that fit a power law distribution as determined using the method of *Clauset et al.* [2009]. Scan series A clasts range from 2.16 mm to 13.45 mm, series B clast sizes range from 2.68 mm to 14.50 mm, series F clast sizes range from 0.45 mm to 10.03 mm, and series P clast sizes range from 9.37 mm to 59.87 mm. The power law scaling parameter for each series is 2.81, 2.99, 2.99, and 3.13 respectively. Cumulative frequency is normalized by the total volume of fault gouge scanned in each series. Series P, with permission is particle size data collected by *Sills* [2010] of the combined SDZ and CDZ core sections imaged at low resolution at the Harold Vance Department of Petroleum Engineering X-Ray Computed Tomography Facility at Texas A&M University.

Table 4. Comparison of particle size parameters with and without excluded clasts.

Dataset	Number of clasts	Upper bound (mm)	Lower bound (mm)	Power Law scaling parameter (n)	Goodness of fit (p)
series A (all)	5229	13.40	2.21	3.02	0.74
series A (+excluded)	5279	13.45	2.16	2.81	0.53
series B (all)	3448	14.50	2.68	3.09	0.71
series B (+excluded)	3473	14.50	2.68	2.99	0.54
series F (all)	4101	10.03	0.45	2.99	0.89
series F (+excluded)	4141	80.74	0.39	2.68	0.20

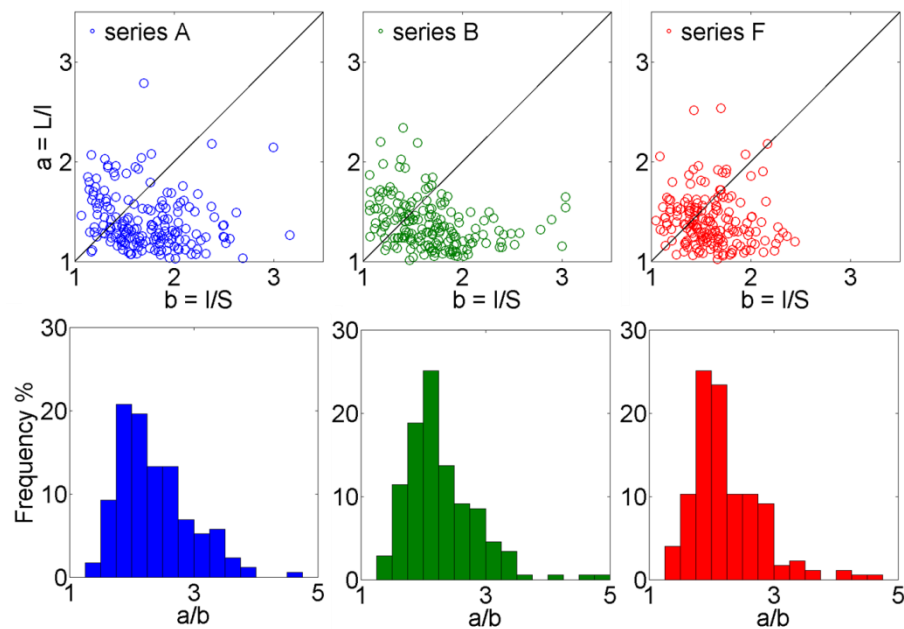


Figure 17. Shape of best-fit primitive ellipsoids to survivor clasts from the SDZ for series A, B, and F plotted in a Flinn diagram. Shapes are defined by the ratios of the long to intermediate axes and the intermediate to short axes of the primitive fit ellipsoid. In the diagram, perfect spheres plot at the origin, and prolate ellipsoids are plotted above the one-to-one line while oblate ellipsoids are plotted below the one-to-one line. The percent frequency histograms represent the statistical shape distribution in terms of aspect ratio.

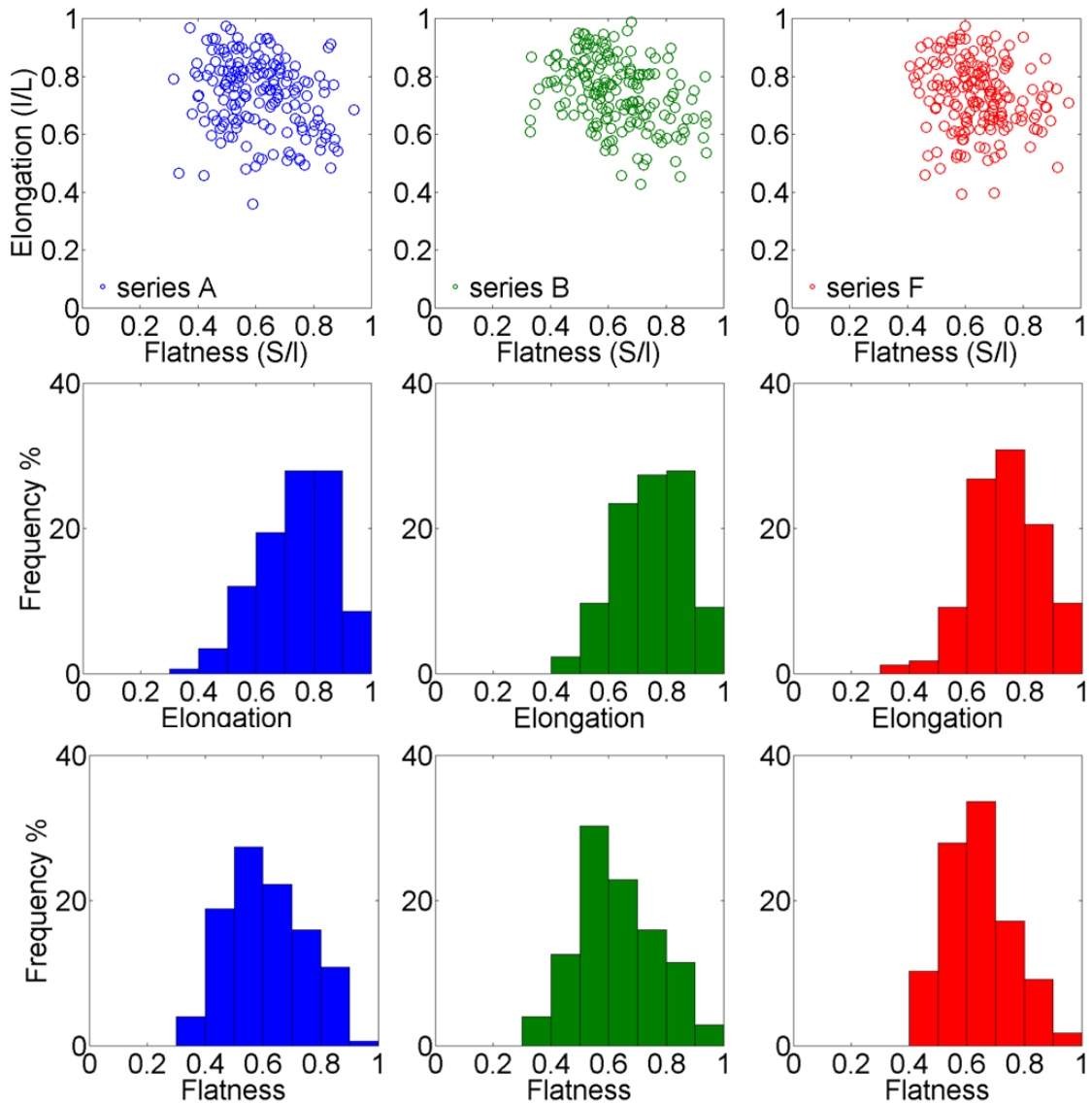


Figure 18. Shape of best-fit primitive ellipsoids to survivor clasts from the SDZ for series A, B, and F plotted in a Zingg diagram. Shapes are described by the ratios the intermediate to long axes and the short to intermediate axes of the primitive fit ellipsoid. The percent frequency histograms represent the statistical shape distributions of elongation and flatness for each series.

Table 5. Classification and distribution of clast shape.

Type	series A %	series B %	series F %	Description
T1	0	0	0	Discoid Very oblate
T2	3	4	0	spheroid
T3	41	41	31	Oblate spheroid Sub-equant
T4	38	41	55	spheroid
T5	2	2	2	Equant spheroid
T6	6	2	7	Blade
T7	10	10	5	Prolate spheroid
T8	0	0	1	Roller

Table 6. Shape parameters percentages by value ranges.

	series A	series B	series F
Elongation			
Class 5 (0.0 - 0.2)	0%	0%	0%
Class 4 (0.2 - 0.4)	1%	0%	1%
Class 3(0.4 - 0.6)	15%	12%	11%
Class 2 (0.6 - 0.8)	47%	51%	58%
Class 1 (0.8 - 1.0)	37%	37%	30%
Flatness			
Class 5 (0.0 - 0.2)	0	0	0%
Class 4 (0.2 - 0.4)	4%	4%	0%
Class 3 (0.4 - 0.6)	46%	43%	38%
Class 2 (0.6 - 0.8)	38%	39%	51%
Class 1 (0.8 - 1.0)	11%	14%	11%
Equancy			
Class 5 (0.0 - 0.2)	1%	0%	0%
Class 4 (0.2 - 0.4)	34%	28%	27%
Class 3 (0.4 - 0.6)	57%	62%	61%
Class 2 (0.6 - 0.8)	6%	10%	13%
Class 1 (0.8 - 1.0)	0%	0%	0%
Convexity			
0.0 - 0.2	0%	0%	0%
0.2 - 0.4	0%	0%	0%
0.4 - 0.6	5%	4%	2%
0.6 - 0.8	54%	60%	29%
0.8 - 1.0	41%	36%	69%
Sphericity			
0.0 - 0.2	0%	0%	0%
0.2 - 0.4	0%	0%	0%
0.4 - 0.6	3%	3%	0%
0.6 - 0.8	41%	31%	36%
0.8 - 1.0	55%	66%	64%

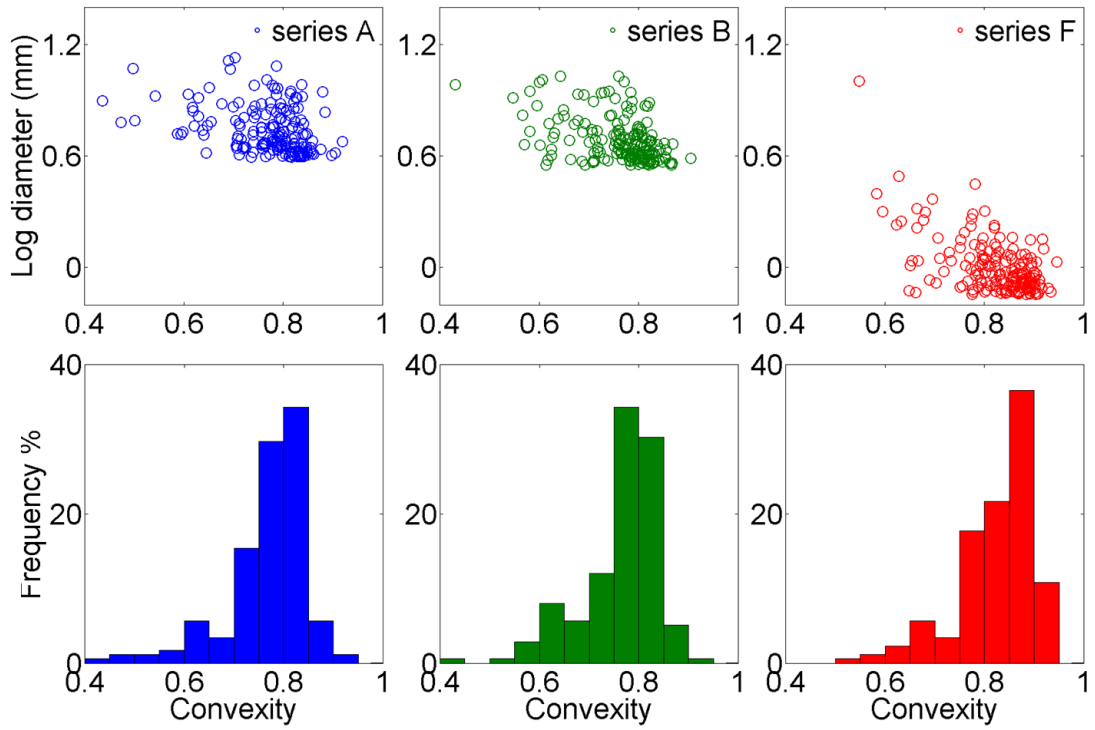


Figure 19. Scatter plots of log equivalent spherical diameter versus convexity for survivor clasts from the SDZ for series A, B, and F. Histograms show the percent frequency distribution of convexity for series A, B, and F.

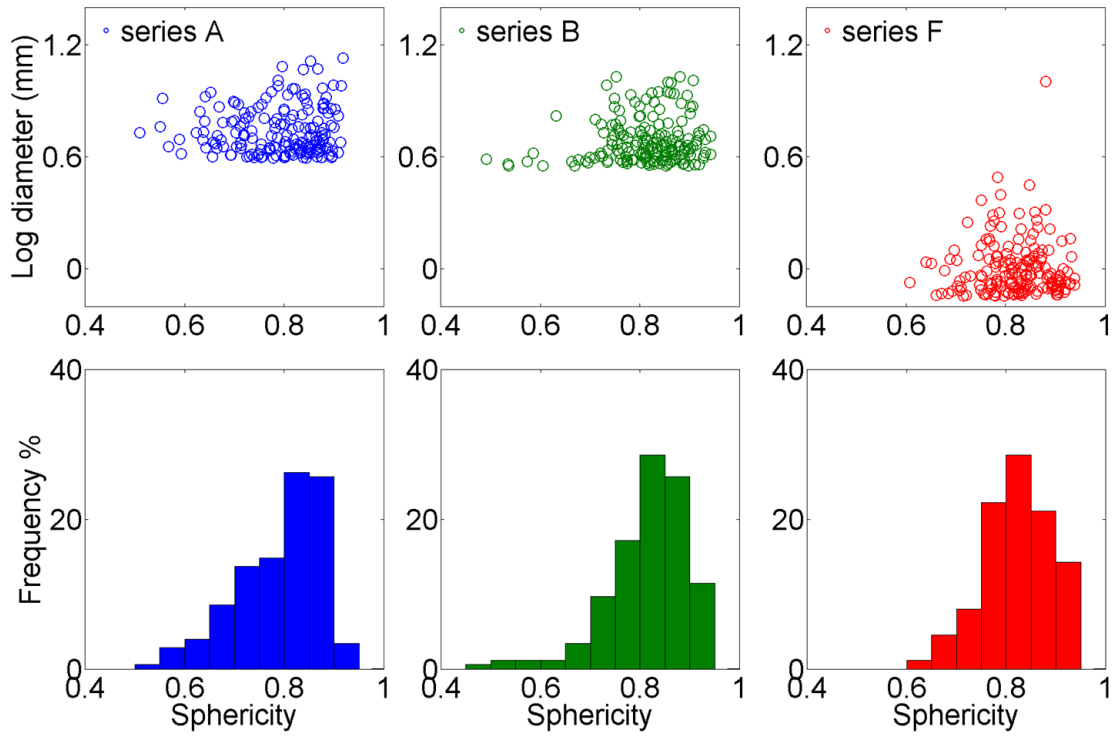


Figure 20. Scatter plots of log equivalent spherical diameter versus sphericity for survivor clasts from the SDZ for series A, B, and F. Histograms show the percent frequency distribution of sphericity for series A, B, and F.

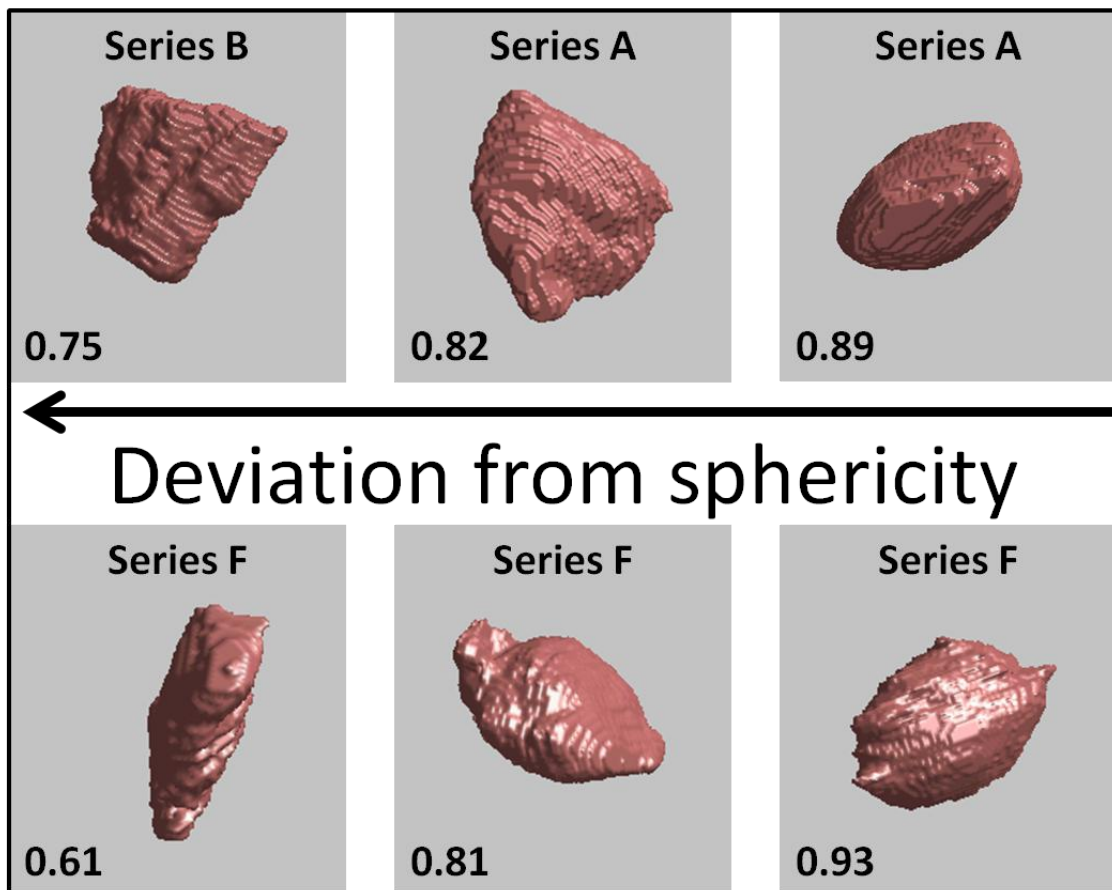


Figure 21. Sample of clast shapes with corresponding sphericity values. Clasts from series A and B range in size from 9.1 mm to 10.7 mm in diameter. Clasts from series F range in size from 0.9 mm to 1.5 mm in diameter.

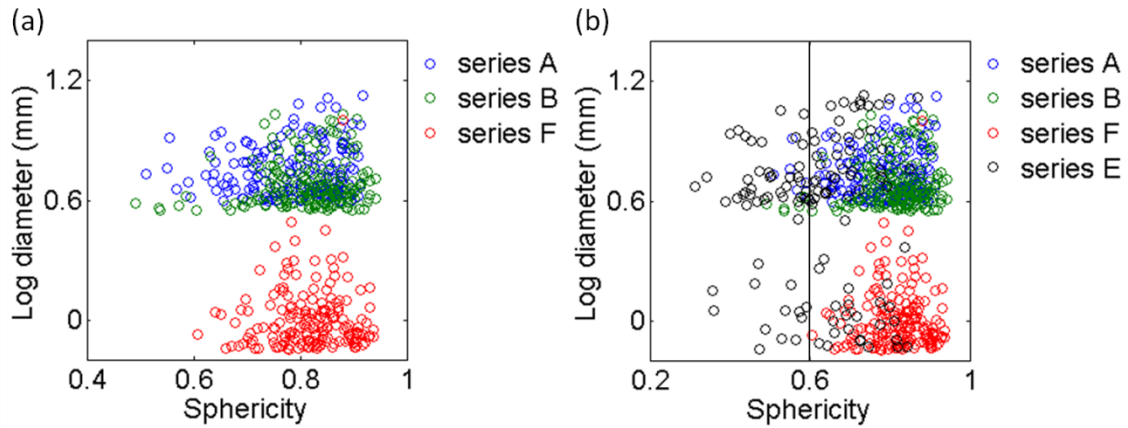


Figure 22. Scatter plots of log equivalent spherical diameter versus sphericity showing the result of adding the excluded clasts to the data sets of scan series A, B, and F of the SDZ. (a) Scatter plot of series A, B, and F. (b) Scatter plot of series A, B, F and E. Series E is a collection of all clasts that are excluded from series A, B, and F. Notice the majority of clasts from series E have sphericity values less than 0.6.

Table 7. Shape distributions with 99.9% confidence where value of 0 is statistically the same and value of 1 is statistically different.

	Convexity	Sphericity	Elongation	Flatness	Aspect Ratio
series A & B	0	0	0	0	0
series A & F	1	0	0	1	0
series B & F	1	0	0	0	0

Table 8. File naming convention.

File Name	Image description
SDZ_G2S7a_Cal SDZ_G2S7b_Cal	Calibrated images set all pixel values outside of the sleeve of the core sample to black and a white pixel is placed in the top right corner of the image.
SDZ_G2S7a_Mask SDZ_G2S7b_Mask	Mask images are result of a second degree polynomial fit to the radial profile of the calibrated images.
SDZ_G2S7a_Cal_ilcor SDZ_G2S7b_Cal_ilcor	Illumination corrected images are the result once the mask is subtracted from the calibrated image.
SDZ_G2S7a_Cal_ilcor_filt SDZ_G2S7b_Cal_ilcor_filt	Filtered images are the result of a weighted neighbor threshold with a black background/matrix and white survivor clasts.

APPENDIX B
XCT IMAGE CORRECTION

The following outlines the methods implemented in Matlab to correct the XCT images that are used in this study to identify survivor clasts within a gouge matrix.

B.1 Calibrate Grayscale Images

In order to for slice images to keep a consistent local minimum and maximum value, each 16-bit tiff image is calibrated with a black pixel (value 0) and white pixel (value 65536). The m-file created to perform this step is named *Calibrated_AL.m*. A global m-file used to run several functions (such as *Calibrated_AL.m*) automatically for each scanned series is named *Auto_Read_Write_AL.m*. The input file is SAFODXXXX.tif and SAFODbXXXX.tif for series A and series B, respectively. The corresponding output file is G2S7aXXX_cal.tif and G2S7bXXXX_cal.tif, where XXXX refers to the slice number.

B.2 Create Mask to Correct for Uneven Illumination.

The output data of the mask is G2S7aXXXX_Mask.tif and G2S7bXXXX_Mask.tif.

B.2.1 Determine Center of Illumination

In imageJ I review a subset of images using an interval of 20 to determine the center of illumination. I used the following method:

1. In ImageJ, import the subset of images. To do this select *File-Import-Image Sequence*. Open the folder with the calibrated images, click on any image and the *Sequence Options* box will open. Set the *increment* to 20.
2. Choose a level and window which will be the same for the entire review process. The Level/window chosen is 26111/1792. To do this, click on *Image-Adjust-Window/Level*.

3. Determine the bounds of the bright center by drawing a square following the gradient edges where illumination is mostly uniform. To do this use the *Rectangle selection*. When determining the bounds, it is important to not be influenced by the outer sleeve and large bright clasts.
4. Apply the plugin *Concentric Circle* to the first image and record the center (X,Y) position in an excel sheet. The plugin is downloaded from <http://rsbweb.hih.gov/ij/plugins/concentric-circles.html> and is placed in *.class* file in the ImageJ *Plugins* folder. To do this make sure the rectangle from step 3 is highlighted, then click on *Plugins-Concentric Circles*.
5. Traverse through the scanned core keeping the same center (X,Y) until there is a change in center position. Repeat steps 3 and 4 until a center (X,Y) is recorded for the entire subset. The center (X,Y) for all images are recorded in an excel file where the first, second, and third column is image number, center X, and center Y, respectively.
6. Each slice will have a center point based on the subset center data points. To do this, the first subset image center is applied towards all images until the next image from the subset, then the new subset image center is applied towards the next set of images and so forth. This is automated using the *Center_Point_AL.m* m-file. The input (File,Sheet,Range) is *Image_Correction_AL.xls,SDZ_G2S7a,A:C* and the output is *Image_Correction_AL.xls,SDZ_G2S7a,E:G* for series A. Series B is similar but the Sheet name changes to *SDZ_G2S7b*.

B.2.2 Determine Center of Core

1. Using the same images subsets, draw a circle to match the core boundaries. To do this click on the *Oval Selection*. This circle will be a baseline for all subsequent images.
2. Apply the plugin *Concentric Circle* to the first image and record the center (X,Y) position and radius in an excel sheet. The plugin is downloaded from <http://rsbweb.nih.gov/ij/plugins/concentric-circles.html> and is placed in *.class* file in the ImageJ Plugins folder. To do this make sure the circle from step 1 is highlighted, then click on *Plugins-Concentric Circles*.
3. Move the circle created in step 2 to keep a consistent core boundary. This method will record a new center (X,Y) while maintaining a equal radius for all center picks. Traverse through the scanned core keeping the same center (X,Y) until there is a change in center position. Repeat steps 1 and 2 until a center (X,Y) is recorded for the entire subset. The center (X,Y) for all images are recorded in an excel file where the first, second, and third column is image number, center X, and center Y, respectively.
4. Each slice will have a center point based on the subset center data points. To do this, the first subset image center is applied towards all images until the next image from the subset, then the new subset image center is applied towards the next set of images and so forth. This is automated using the *Center_Point_AL.m* m-file. The input (File,Sheet,Range) is Image_Correction_AL.xls,SDZ_G2S7a,A:C and the output is

Image_Correction_AL.xls,SDZ_G2S7a,E:G for series A. Series B is similar but the Sheet name changes to SDZ_G2S7b.

B.2.3 Identify Uniform Images for Unbiased Radial Profiles

Scan through images using an interval of 20 and exclude images that are highly variable due to large bright clasts, missing material, highly sheared material, etc. The following image slice numbers are used to determine:

1. Foliated Cataclasite (a0141, a0161, a0181, a0201)
2. Upper Gouge (a0521, a0541)
3. Lower Gouge (b0581, b0601, b0621, b0641, b0741, b0761, b0781, b0801)
4. Serpentinite (a1021, a1041, b0001, b0021, b0041, b0061, b0081, b0101, b0221, b0241, b0261, b0281, b0301, b0321)

B.2.4 Record the Radial Profile Given the Center and Radius

1. Using the same images subsets, determine the radial profile in Matlab using the m-file *Radial_Profile_Test_AL.m*, which calls on the modified function *rscan.m* created by Narupon Chattrapiban. Modification includes not normalizing the data.
2. Record the profiles in excel and take the average of each subset (Foliated Cataclasite, Upper Gouge, Lower Gouge, and Serpentinite). The output (filename, sheet) is *Radial_Profile_Test_AL.xls*, 070214_redo,072014_avg. The columns for Foliated Cataclasite is B:F and the average is F, Upper Gouge is H:J and the average is J, Lower Gouge is L:T and the average is J, and Serpentinite is V:AJ and the average is AJ.

B.2.5 Determine the Least Squares Best Fit Second Degree Polynomial Equation

A transformation of the radial profile values is required to create the mask in Matlab with the top left corner as the origin (versus the output profile which assumes the bottom left corner is the origin). Since I was only interested in the Upper and Lower Gouge, I average these profiles and the excel best fit equation is

$$y(r) = -0.0102r^2 + 26216$$

The equation used to create the mask is

$$y(r) = -0.0102r^2 + C^*$$

which includes a normalizing value C^* defined by

$$C^* = y(r)|_{r=0} - y(r)|_{r_{\max}}$$

The region outside of r_{\max} is set to black (0 pixel value).

B.3 Create Corrected Images

In order to create a corrected uneven illumination image, I subtract the mask from the calibrated data. This step is coded in the m-file *Auto_Read_Write_AL.m*. The input files are G2S7aXXXX_Cal.tif and G2S7bXXXX_Cal.tif and G2S7aXXXX_Mask.tif and G2S7bXXXX_Mask.tif and the output files are G2S7aXXXX_Cal_ilcor.tif and G2S7bXXXX_Cal_ilcor.tif.

B.4 Create Binary Images

Binary images are created using the *Filter_AL.m* file. The input images are G2S7aXXXX_cal_ilcor.tif and G2S7bXXXX_cal_ilcor.tif. The output data of the binary images are G2S7aXXXX_cal_ilcor_filt.tif and G2S7bXXXX_cal_ilcor_filt.tif. I used the following method:

B.4.1 Remove Noise Pixilation

Noise pixilation is removed using a 10 x 10 median filter

B.4.2 Determine a Threshold Value

In Matlab, through trial and error, I determine a threshold value using the following method:

1. Randomly select a few sample images, then randomly selection portions of the core containing matrix and clasts while excluding black pixels (0 pixel value).

Run the function *Graythresh* in Matlab. *Graythresh* determines a value from 0 to 1.

1. Once this value is determined, I multiply the graythresh value by 65536 in order to get a 16-bit threshold value. This is done using the function *Filter_AL.m*.
2. Step 1 is repeated several times to determine a threshold value that works for all scans. The threshold value used for series A and series B is 25186 and 25445, respectively.

B.4.3 Use a Weighted Neighbor Threshold

1. The weighted neighbor threshold value looks at each pixel's local 8 neighbors, doubles the value of the center pixel (hence weighted) and takes the average of all 9 pixels. If the average pixel value is less than the threshold value, the pixel is set to black (0 pixel value), otherwise, the pixel is set to white (1 pixel value), resulting in a binary image.

APPENDIX C

FABRICATED SAMPLE CLAST SELECTION PROCESS

The following outlines the methods implemented in Matlab to select clasts within fragments of the fabricated sample and to record an accurate volume of gouge. The fabricated dataset is referred to as series F. The following m-files are used:

Calibrated_AL.m, *Fragment_AL.m*, *Mask_f_AL.m*, *Threshold_f_AL.m*, and *Auto_Read_Write_AL.m*.

C.1 Calibrate Grayscale Images

In order to for slice images to keep a consistent local minimum and maximum value, each 16-bit tiff image is calibrated with a black pixel (value 0) and white pixel (value 65536). The m-file created to perform this step is named *Calibrated_AL.m*. A global m-file used to run several functions (such as *Calibrated_AL.m*) automatically for each scanned series is named *Auto_Read_Write_AL.m*. The input file is G2S7fXXXX.tif in the folder SDZ_G2S7_f_Original. The corresponding output file is G2S7fXXXX_cal.tif in the folder SDZ_G2S7_f_Calibrated, where XXXX refers to the slice number.

C.2 Create Fragment Mask

In order to create a fragment mask, I set the epoxy (12680 pixel value) to black (0 pixel value). The threshold value for epoxy is determined by inspection in ImageJ. The input file is G2S7fXXXX_cal.tif in the folder SDZ_G2S7_f_Calibrated. The corresponding output file is G2S7fXXXX_cal_frag_binary.tif in the folder SDZ_G2S7_f_Fragments.

C.3 Create Binary Fragment Mask

I create an image showing only the largest fragments and threshold the image to be binary. This image will be used to isolate only the clasts found within the largest 200 fragments. First I decide the limiting size by removing interconnected pixels less than and equal to 25,000 pixels. The pixel value is determined through trial and error. I found that setting the interconnect pixel value to 10,000 resulted in 300 of the largest fragments and setting the value to 40,000 resulted in the largest 140 fragments. In order to determine how many fragments were captured, I had to complete all step including the Blob3D process (refer to Appendix D). I chose a value in between to get the 200 largest fragments. The input folder is SDZ_G2S7_f_Fragments, and the corresponding output folder is SDZ_G2S7_f_Fragments_Binary.

C.4 Create Largest Fragment Image

The largest fragment images are created using the *Mask_f_AL.m* file. This step requires both the Fragment Mask and the Binary Fragment Mask as input images. The images are multiplied and the resulting image is black (0 pixel value) everywhere except for the 16-bit grayscale pixel values within the largest fragments. The output file is G2S7fXXXX_cal_frag_mask.tif in the folder is SDZ_G2S7_f_Fragments_Large.

C.5 Create Binary Image of Only Clasts within Fragments

Binary clast images are created using the *Threshold_f_AL.m* file. The input images G2S7fXXXX_cal_frag.tif and G2S7fXXXX_cal_frag_mask.tif from the folders SDZ_G2S7_f_Fragments and SDZ_G2S7_f_Fragments_Large respectively. The output

data of the binary images are G2S7fXXXX_cal_clast_binary.tif. I used the following method:

C.5.1 Remove Noise Pixilation

Noise pixilation is removed using a 5 x 5 median filter

C.5.2 Determine a Threshold Value

In Matlab, through trial and error, I determine a threshold value by inspection. Over the range of slices 500-1000, the clasts grayscale pixel value ranged from 13660 – 13680 which appear to be nearly the same. The threshold chosen for this series was 13660.

C.5.3 Use a Weighted Neighbor Threshold

The weighted neighbor threshold value looks at each pixel's local 8 neighbors, doubles the value of the center pixel (hence weighted) and takes the average of all 9 pixels. If the average pixel value is less than the threshold value, the pixel is set to black (0 pixel value), otherwise, the pixel is set to white (1 pixel value), resulting in a binary image.

APPENDIX D
BLOB3D PROCESS

The following outlines the methods implemented in Blob3D to correct the XCT images that are used in this study to isolate and separate survivor clasts within a gouge matrix. IDL Virtual Machine is required as well as the file BLOB3D.sav which can be obtained from

D.1 Three-Dimensional Reconstruction of Survivor Clasts

Survivor clasts from each series are reconstructed in 3D using the following method:

D.1.1 Setup the Parameters

1. From IDL Virtual Machine run the file Blob3D.sav.
2. Import image from the folder. To do this, click on the *Load Tiffs* button. A window prompt request the inter-pixel spacing (mm) and inter-slice spacing (mm) values. For series A and B the values are 0.116 and 0.45, respectively. For series F the values are 0.02892 and 0.0266, respectively.
3. Click on *List Components* and input *porphyroclasts* as the component.
4. Click on *Segment-General Threshold* and change the lower bound threshold from 0 to 1. Then click on *Process all data*.

D.1.2 Clast Segmentation

1. Click on *Separate*. Then change the voxel size (automatically set to 6) to 165 (to have a minimum diameter of 1 mm).
2. Open several windows to view the blob including: 3D, Z (at scale 1x and 2x are helpful), X and Y are optional.

3. For each blob you have the option to: accept all, delete all (I delete clasts touching the border if obvious), and separate.
4. There are two methods of separation: Erode and Dilate or Pick 3. For Pick 3, click on the blob with the mouse (on the 3D window) and create a plane of division separating two or more touching clasts.
5. Save progress often and be sure to save the last state with .sav at the end of the file name.
7. Using Blob3D, 3D reconstruction of survivor clasts are created from each series (A and B).

D.1.3 Data Extraction

Data parameters take a long time to extract so it is recommended to only extract 1-2 parameters at a time. The parameters used are: volume, surface area, and fit primitive.